

N O T I C E

THIS DOCUMENT HAS BEEN REPRODUCED FROM
MICROFICHE. ALTHOUGH IT IS RECOGNIZED THAT
CERTAIN PORTIONS ARE ILLEGIBLE, IT IS BEING RELEASED
IN THE INTEREST OF MAKING AVAILABLE AS MUCH
INFORMATION AS POSSIBLE

HEAT GENERATION IN AIRCRAFT TIRES
UNDER FREE ROLLING CONDITIONS

A Report prepared for

National Aeronautics Space Administration
Langley Research Center
Hampton, Virginia

(NASA-CR-164273) HEAT GENERATION IN
AIRCRAFT TIRES UNDER FREE ROLLING CONDITIONS
(Michigan Univ.) 90 p HC A05/MF A01

N81-23461

CSCL 01C

G3/37 Unclass
42260

Samuel K. Clark
Richard N. Dodge

Department of Mechanical Engineering
and Applied Mechanics
University of Michigan
Ann Arbor, Michigan
December 1980



INTRODUCTION

The development of heavy transport and military aircraft with high performance characteristics has placed increased demand on landing gear and tire components. Specifically, aircraft tires have developed through the years to a point where the ratio of tire weight to aircraft weight has steadily decreased. In part this is due to improved tire cord materials, tire compounds and tire structural design, but in addition it has resulted from the use of aircraft tires closer and closer to their ultimate limit. This has resulted in a need for development of methods for predicting the strength limit of aircraft tires on some rational basis other than indoor dynamometer testing.

This problem of tire strength is not one such as is encountered in the strength of normal metallic structures. The reasons for this lie in the complexity of the material characteristics of the constituents in an aircraft tire. There are several factors at work here. First of all is the direct problem of loading of structure in the usual sense. In an aircraft tire almost all loads are carried directly by the textile cord structure of the tire, commonly nylon as is presently practiced. There are some compressive loads carried by rubber elements in the tread but these are rather minor. In addition to the strength problem, aircraft tires generate substantial temperatures as they roll, both during takeoff and landing. The temperatures are not high in the usual sense of metallic materials, being of the order of hundreds of degrees Fahrenheit or less, but they are high enough to seriously degrade the strength of the load carrying textile components in the tire. Excessive temperatures can easily cause a tire to fail even if the stress levels are not overly high.

In addition to the interaction of temperature and stress, even more complex phenomena are at work in the repeated daily use of aircraft tires. These phenomena are basically associated with the long term strength and adhesion degradation of an aircraft tire due to both stress and temperature, operating cyclically as the aircraft tire is used in a cyclic sense, as well

as the interaction of stress and temperature in such long term strength degradation. This is an area where not much hard information is available, and represents a region where the field usage of tires must depend on experience and judgment rather than upon science. Because of this strength degradation factor, the useful life of aircraft tires is limited, but these limits are not clearly defined and they vary from one aircraft to another and from one airline operator to another.

At the present moment there are substantial advances being made in the tire industry in calculating stresses imposed on textile cord structures due to loading of a tire, such as inflation and load carrying. However the area of tire temperature build up, which is the second major cause of tire failure, has been almost untouched and at the present moment there is no analytical technique suitable for predicting aircraft tire internal temperatures on a rational basis. This means that the tire designer or manufacturer is not able to compare the anticipated temperature build up in a new design with previous designs or with known temperature-strength characteristics of the materials which he wishes to use. This is a serious shortcoming in the design process, and is furthermore a serious shortcoming in the process of preliminary design of transport aircraft, where a knowledge of anticipated higher temperatures during normal take off and landing cycles would be an important asset in assessing the validity of proposed tire, aircraft weight and ground speed combinations.

For these reasons, the present research effort is directed toward construction of a rational method for evaluating internal temperatures of an aircraft tire and for calculating these rapidly and easily so that the method may be used as a design tool in both the tire and airframe industries.

SUMMARY

A method has been developed for approximating the internal temperature distribution in an aircraft tire due to free rolling under load in a straight line. The method is based on the concept of using an approximate stress analysis of a material point in the tire as it rolls through the contact patch and out into the region free of contact. From this approximate stress analysis the mechanical work done on this material point can be converted into the heat generated due to the loss characteristics of the materials at that point. This means that each material point of the tire will have its own cyclic heat generation each time it rolls through the contact patch and is stressed.

Due to the high frequency of cyclic stressing compared with the relatively slow diffusion times of heat in polymeric materials, the temperature distribution in the tire is considered to be axisymmetric.

With a rate of heat generation established at each material point on a cross section of the tire, heat diffusion throughout the carcass can be calculated by the usual numerical methods which will, of course, involve loss of heat in the tire through various mechanisms such as convection at the outer and inner surfaces, conduction through the bead area into the flange of the wheel, and conduction through the tread surface into the runway material. All of these mechanisms modify the normal diffusion process so that at any time, tire internal temperatures are dependent not only upon internal rates of heat generation but also on the appropriate loss characteristics at the tire surfaces.

An extensive experimental program has been carried out jointly between the University of Michigan and the Impact Dynamics Branch, Langley Research Center, NASA. This program consisted of temperature measurements made at internal points in a number of 22 x 5.5 8PR and 22 x 5.5 12PR aircraft tires. Most of the experimental data was taken at the NASA Wallops Island Test Facility. This was done using the NASA tire test truck, and the tires were operated on

a concrete runway surface. The University of Michigan data was taken on the 120 inch dynamometer drum at Wright Patterson AFB, Ohio, where higher tire loads could be obtained.

All data was obtained by thermocouples buried in the tire carcass prior to retreading the tires. These thermocouples were connected to conventional recording apparatus, and gave continuous readings of tire temperature at selected internal points.

Experimental data from these measurements is compared with calculation over a wide range of tire loads, inflation pressures, speeds and deflections. Generally speaking the analytical model proposed here gives good agreement of calculation with measured values when the tire is operating in the range of its normal rated load, pressure and deflection. When the tire is seriously under-inflated the theory predicts lower temperature rise than is observed, and this aspect of it requires further work.

GEOMETRY OF TIRE DEFORMATION

The basic material property being used in the development of this computational method is the hysteretic loss characteristic of polymeric materials during cyclic stressing. This is best illustrated in Figure 1, where a typical stress strain curve for a lossy material is illustrated. As material is stressed from point A to point B and return in Figure 1, the stress-strain curve on the loading cycle does not coincide with the stress-strain curve on the unloading cycle, and the net resulting area under the curve which remains as the material is returned to its original stress state, point A as illustrated in Figure 1, represents a loss of mechanical work during the cycle from A to B and

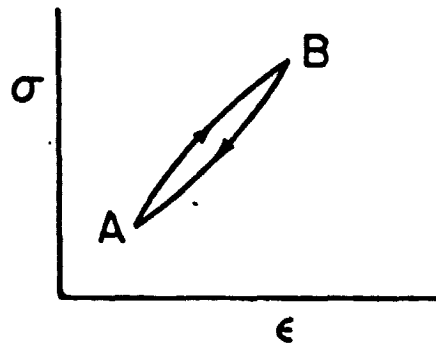


Fig. 1. Typical stress-strain curve of a material illustrating hysteretic loss

return. This lost work is converted into heat and is either diffused through the element and eventually lost from its surfaces or must be accounted for in some way in a heat balance. From the analytical point of view, the work done in a stress cycle as experienced by a material point in passing through the contact patch is expressed most usefully by the use of a simple linear viscoelastic model such as the Kelvin-Voigt solid, and using such a model the energy loss per cycle may be written as in Equation 1.

$$\Delta E = U \pi \Delta V \cdot \tan \delta \quad (1)$$

where

- ΔE = Energy loss/cycle
- U = Change in Strain Energy from A to B
- $\tan \delta$ = Loss Tangent of Material
- ΔV = Volume Element

This formulation presumes that the initial stress induced by tire inflation has no influence in a linear sense on the energy loss per unit stress cycle, and this may be shown directly by computation. However, the initial stress state may influence the material characteristics, which are not linear in this case. Methods for calculating the change in strain energy will be discussed in the next section of this report.

The fundamental method used for calculating the change in strain energy is based on two assumptions. The first is that the tire is made up of a series of material points, each of which undergoes a change in stress state corresponding to the points A and B in Figure 1, as it moves from point A to B shown as in Figure 2.

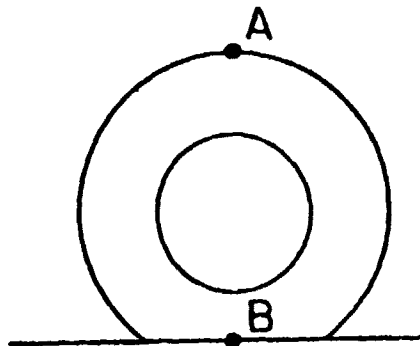
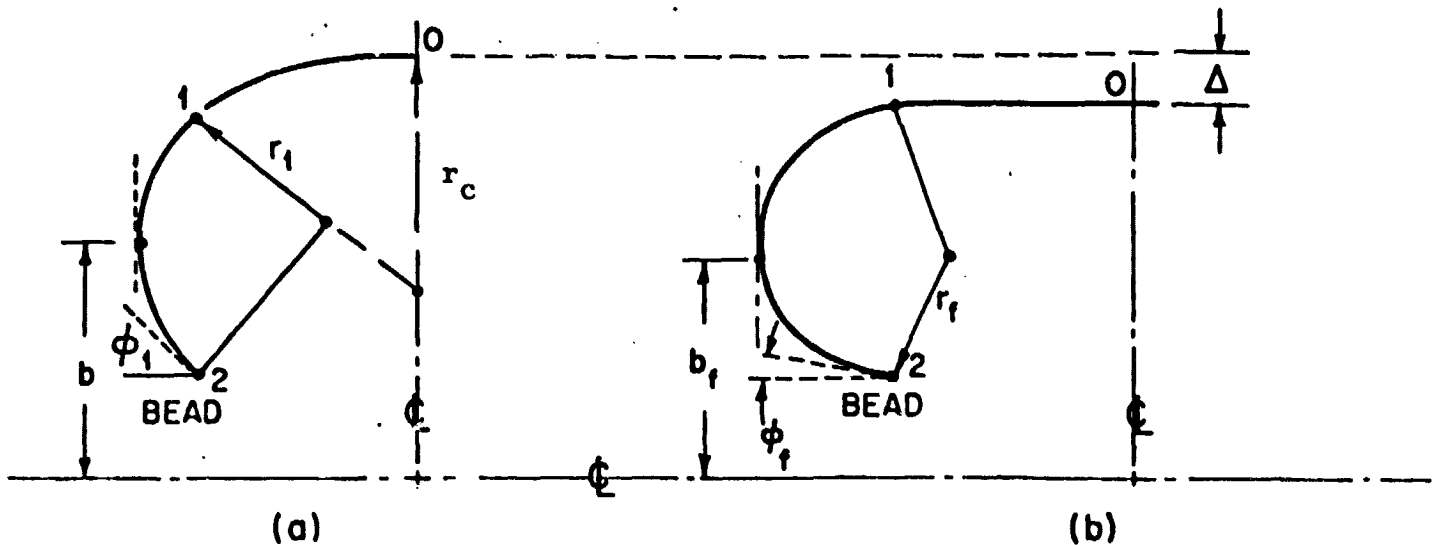


Fig. 2: Extreme points of stress excursion in a tire.

As a material point moves from A to B in Figure 2, we assume that the general wave form of the stress cycle depicted in Figure 1 is unimportant, and we neglect higher harmonics of the cyclic stress in favor of a single fundamental cyclic stress change, which will be described in terms of an assumed geometry of the tire at point A and B. In other words, we make no allowance in

this simplified analysis for a Fourier decomposition of the stress state as the tire moves from A to B, but rather consider only the fundamental harmonic as contributing to the change in strain energy between the two points. This is felt to be a rational assumption in view of the fact that from physical considerations the fundamental must be the primary component, and further that the inclusion of higher harmonics is not warranted within the framework of an approximate analysis such as to be carried out here.

The second major assumption made in calculating the strain energy of the tire as it rolls through the contact patch is that at both points A and B of Figure 2, the cross section of the tire may be represented geometrically by its neutral axis, around which act both membrane and bending strains. This midline representation is assumed to be in the form of circular arcs, as shown in Figures 3A and 3B. The inflated shape of the tire is used to obtain best-fit values for the radii r_1 and r_c , and for their junction points 1 and 2 shown in Fig. 3a.



Assumed geometry at point A, Fig. 2.

Assumed geometry at point B, Fig. 2

Fig. 3

In constructing Figure 3 we illustrate the neutral axis of the structural part of the carcass by the lines labeled 0-1-2. The inflated tire geometry is presumed to be represented by Figure

3a, where a circular arc of radius r_c represents the tread region, while the sidewall region is represented by another circular arc of radius r_1 , tangent to the first arc at point 1. The deformed tire, under deflection Δ as shown in Figure 3b, is presumed to operate under conditions of an indefinitely large radius in sections 0-1, and a reduced radius in the sidewall whose radius of curvature is given by the symbol r_f . The bead, point 2, is fixed. The arcs 0-1 and 1-2 are allowed to shorten in length due to the reduced tension in the sidewall. However, due to the geometry the shortening of 0-1 has little influence on the radius of arc 1-2, and for computational convenience the arc 0-1 is considered inextensible. This allows the complete geometric description of the various radii of curvature, once the tire deflection Δ and once the initial tire geometry are given under inflated conditions. The computational details of the geometric representation are given in Appendix A.

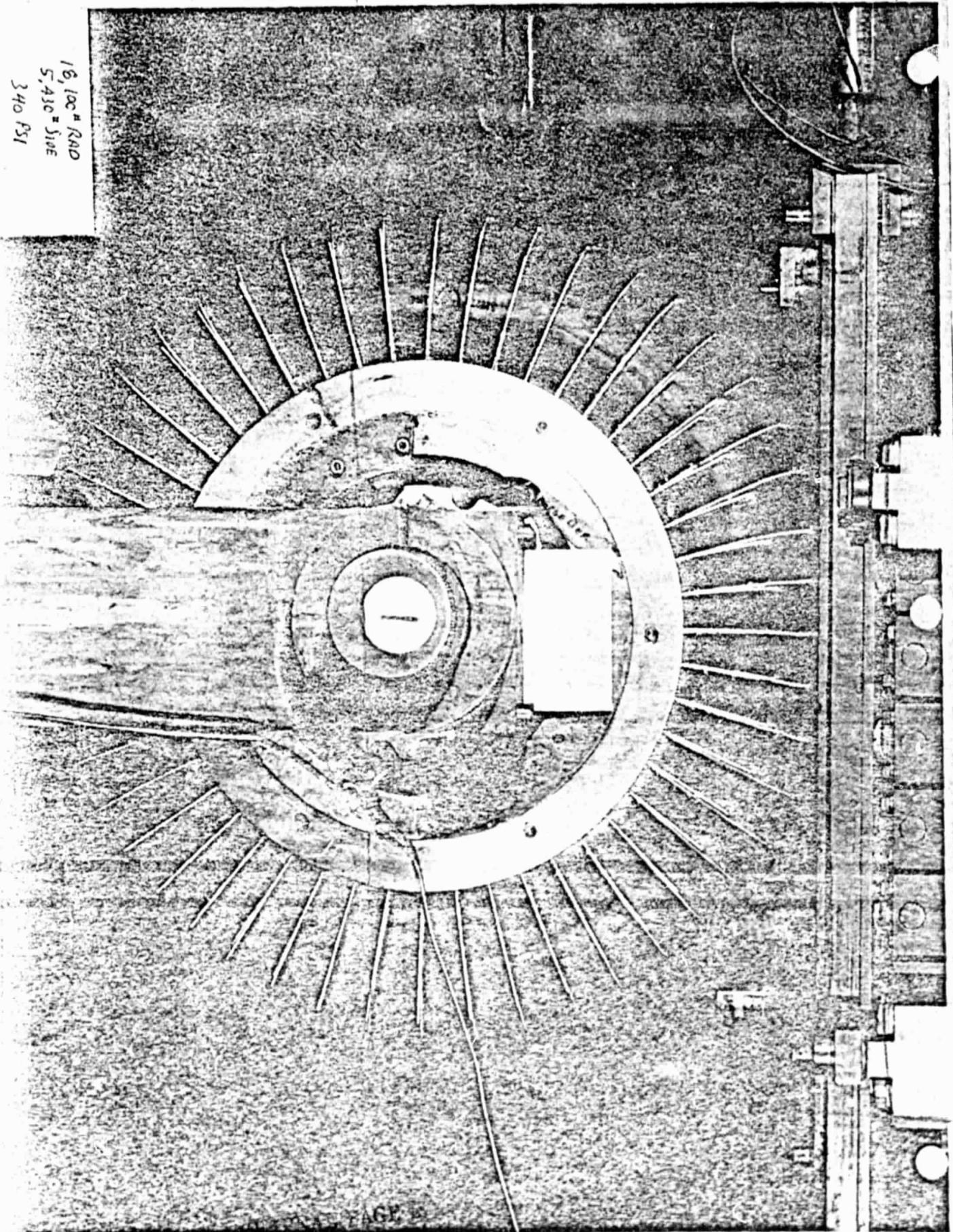
A material point is subject to both bending and membrane strain during deformation of the tire from point A to point B shown in Figure 2. The bending strains are dependent upon the radius of curvature of the midline of the tire carcass as illustrated in Figure 3, as well as upon the distance measured perpendicular from this carcass midline. Denoting this distance by the symbol y , the bending strain can be calculated in the usual linear elastic fashion based on a strength of materials approach, and based upon a knowledge of change in radius of curvature of the carcass midline between the two points in question in Figure 2.

In addition, membrane strains exist in the tire cross section due to the high inflation pressure commonly used in aircraft tires. Some of these membrane strains are not directly obtainable from the geometric changes which have been postulated, since they depend heavily on contact patch boundary conditions. Other membrane strains must be obtained from a knowledge of the membrane stresses in the tire. These membrane stresses in turn depend upon the curvature characteristics of the tire, as well as upon certain geometric variables which may be calculated from the tire cross section geometries given in Figure 3. The details of these calculations are given in Appendix A, where a more complete geometric description

of the tire cross section is derived. In particular, the side wall area must be carefully defined since the point of vertical tangency of the tire is an important factor in computation of membrane stresses. This point of vertical tangency, shown as point B in Figure 3, shifts during the deformation process, and the position of the various material points relative to this point of vertical tangency must be tracked in the subsequent computations.

Due to the fact that aircraft tire deflections are normally large, a further fundamental assumption is that the tire deformation process causes changes in the tire cross section such as shown in Figure 3, such that deformations in the circumferential direction are negligible. This is equivalent to assuming that the tire is actually inflated in a barrel, so to speak, so that axisymmetry of tire displacement is maintained. A typical deformation pattern illustrating this is shown in Figure 4. This imposes the necessity for tracking the radius of a material point from the axis of rotation of the wheel during the deformation process, as shown in Figure 5. The variable used for such measurement is denoted by the symbol z .

16, 100° RAD
5, 430° SIDE
340 PSI



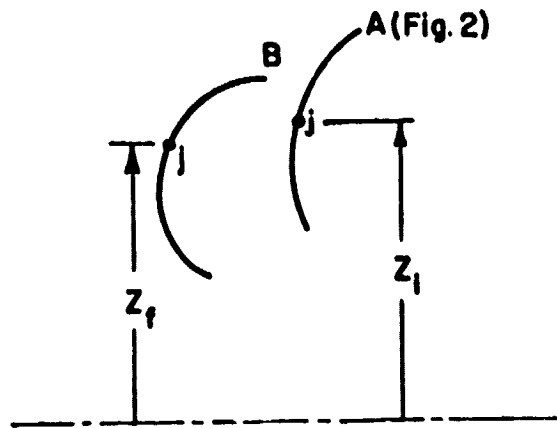


Fig. 5: Tire Cross-Sections

In Figure 5, point j represents a material point which changes axisymmetric radius during the deformation process from A to B. The details of the computation of such change are also given in Appendix A.

Bead tensions also change during the deformation process and must be incorporated into a cyclic stress mechanism involving a loss characteristic of the bead itself. These bead tensions depend on angle of tangency of the side wall at the bead, denoted as point 2 in Figure 3. The details of computations of bead tension are given in Appendix B, where the bead geometry and assumptions governing it are discussed in more detail.

TIRE DEFORMATION AND STRESS

For the calculation of the strain energy change during the rotation of a material point through the contact patch we rely heavily on the assumed tire deformation given in Figures 2-5.

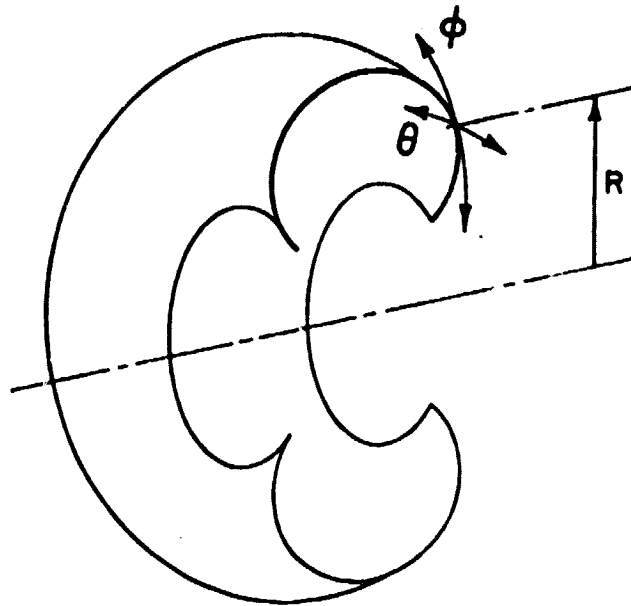


Fig. 6: Tire Coordinate Notation

Figure 6 illustrates the geometry involved and the notation being used here. R represents radial distance from the axis of rotation of the tire, ϕ represents the meridional direction and θ represents circumferential direction.

For purposes of computing changes in strain energy states during the cyclic loading process the tire is divided into five regions, denoted as I-V in Figure 7.

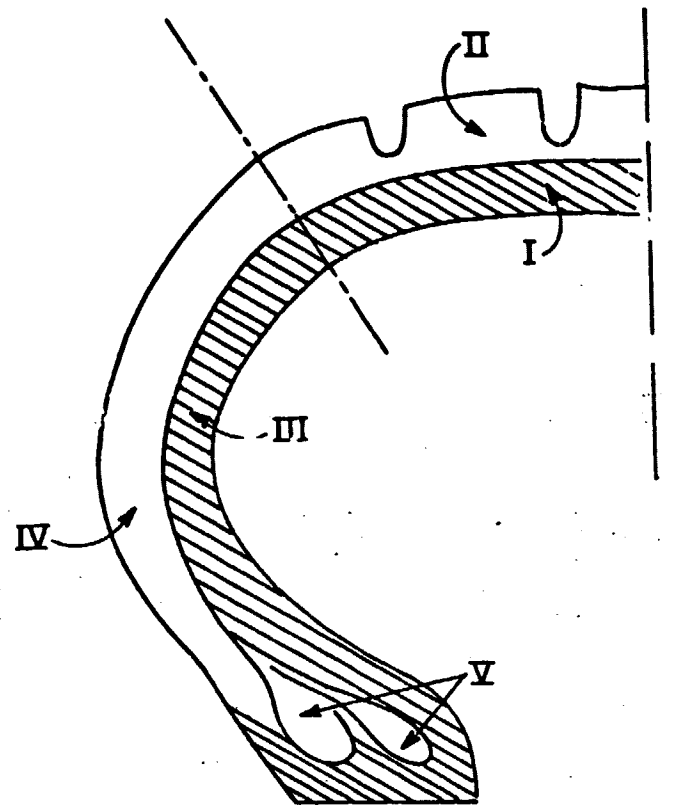


Fig. 7: Tire cross-section showing regions of different characteristics and loading patterns.

The rationale behind the division of the tire into these parts is that region II represents the tread region of the tire, which is considered to be rubber-like and in contact with the runway surface. It is usually characterized by material isotropy and by an elastic shear modulus which is nearly linear up to reasonably large strains. Further, it exhibits near incompressibility, and that fact is used in computing the strain state associated with contact against the runway surface.

The region denoted by I is immediately beneath the tread

region of the tire and is firmly affixed to it, so that the strain state of the two elements in the membrane sense is considered to be equal. However, region I is assumed to be plane orthotropic in its characteristics, and may be thought of as a sheet of material lying in the ϕ - θ plane as illustrated in Figure 8.

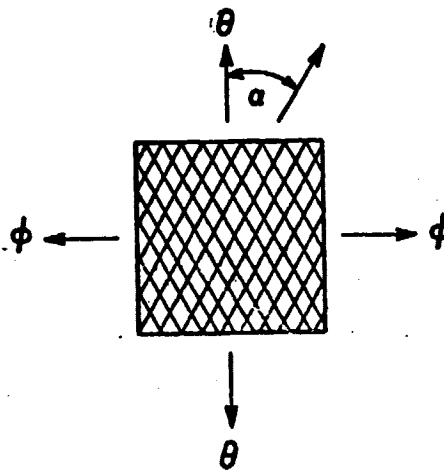


Fig. 8: Laminate characteristics in Region I.

In Figure 8 the diagonal lines represent textile reinforcing cords, which serve to give the primary stiffness to the carcass region. Because of their diagonal character, which is characteristic of a bias aircraft tire, the element shown in Figure 8 will exhibit different elastic constants in the ϕ and θ directions, as well as appropriate shear stiffnesses and Poisson's ratios which are well characterized by the mathematical model of a plane orthotropic material. Such materials have been widely studied in the tire industry and their characteristics can be estimated. Appendix C gives a detailed derivation of the appropriate elastic constants for a plane orthotropic material using the structure shown in Figure 8, adequate to within a range of diagonal reinforcing angles encountered in aircraft tire construction. Figure 8 can be characterized in terms of elastic constants dependent upon the cord reinforcing materials and upon the half-angle α illustrated in the figure.

Regions III and IV of the tire, as illustrated in Figure 7,

represent the side wall areas which are subjected also to changes of curvature as the tire deforms. These areas do not contact the runway surface, so that in region III the carcass strains are again determined and the elastic constants obtained from the model of Figure 8. These are utilized to determine the appropriate strain energy expressions. Region IV represents a rubber covering used primarily as a scuff or abrasion resistant coating on the outside of the tire. It contributes to tire mechanical loss and to the subsequent heat build up, but is not structural in nature. We assume that it is bonded tightly to the carcass of Region III and undergoes the same membrane strains as those of Region III, but in addition undergoes bending strains due to its distance away from the neutral axis, which because of the relatively high textile modulus is usually located in Region III of the carcass.

Finally, the beads of the tire undergo large tension force fluctuations, and these fluctuations must be accounted for separately since they are caused by changing forces in the tire sidewall, which are reacted by the entire bead ring. This requires a separate analysis, not only for the force fluctuation in the bead ring but also because the bead rings are conventionally made of rubber coated steel wire which has significantly different elastic and loss characteristics from the remainder of the tire. For that reason this is denoted as Region V and is handled as a separate analysis.

Because of limited computational ability, we approach the calculation of strain energy stored in the tire during the deformation process by means of splitting each region of the tire into a number of cells, each cell being denoted by a pair of numbers in matrix notation fashion. This is illustrated in Figure 9, where cells are superimposed on the previous Figure 7. The elements shown in Figure 9 are purely for illustration purposes. Any number of elements may be chosen and the order of them may be adjusted to suit the needs of the user, but for the instances to be illustrated numbering begins in the bead area and terminates at the center line of the tire crown. Numbering of the vertical

location of the elements begins at the inner surface and terminates at the tread or outer surface of the tire, as the case may be.

The inner liner of the tire, while pure rubber, is thin enough so that it may be lumped with the composite carcass material.

Computation with the individual elements is facilitated by use of the matrix notation illustrated in Figure 9. However, for a general theoretical treatment of the strain energy change in the tire in this report we will adopt the notation of Figure 7 where the major portions of the tire are delineated. We now give an approximate analysis of each of the regions I-V of the tire.

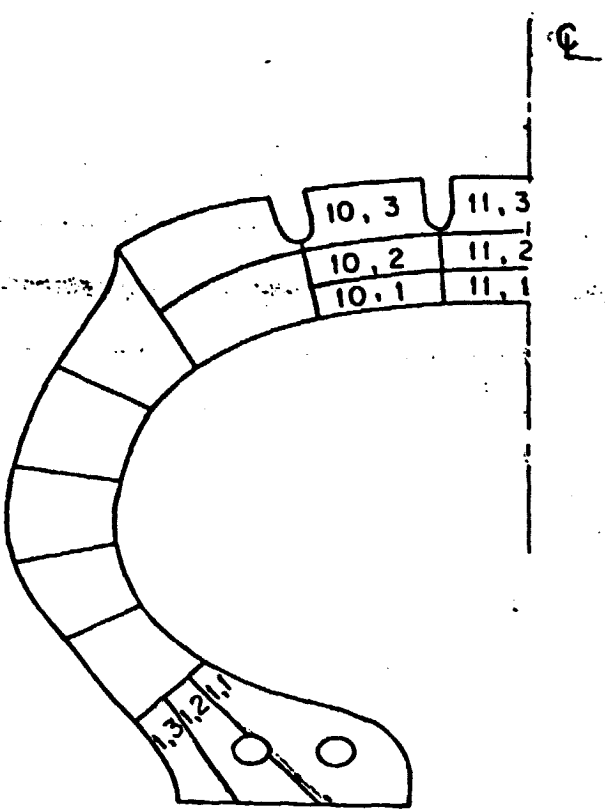


Fig. 9: Element numbering system

Region I

In this section we first used the assumed geometrical changes of Figure 3 to develop membrane strains in the ϕ (meridional) and θ (circumferential) directions. We neglect strains perpendicular to the carcass midline. We include a shear effect to be discussed later.

Consider first a side view of the tire as shown in Figure 10. Recalling the assumption of axisymmetric deformation, we completely restrain all circumferential motion so that the maximum membrane strain in the θ direction occurs at point B and is given by

$$\epsilon_{\theta} = - \frac{\Delta}{R} \quad (2)$$

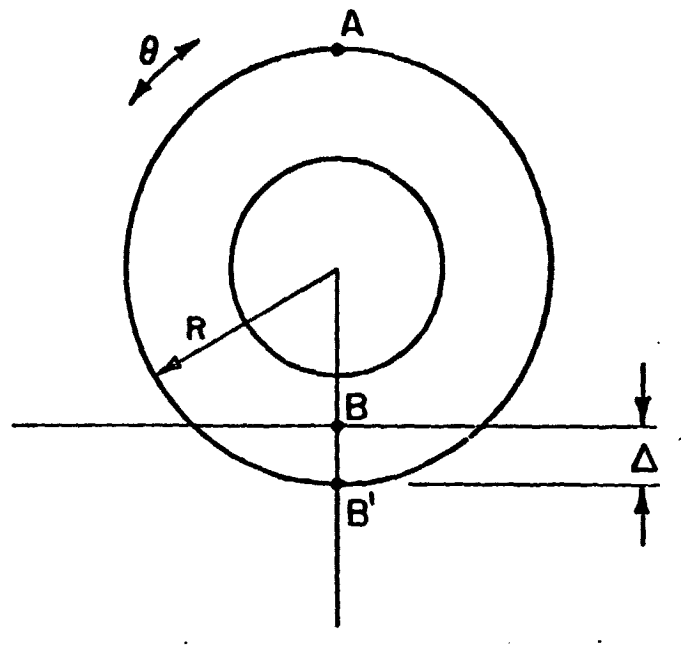


Fig. 10: Side view of tire

In the meridional, or ϕ , direction the situation is more complex since we do not have access to convenient measures of deformation which lead directly to the strain. However the known curvature changes in the sidewall do lead to the membrane stress σ_ϕ , and in particular this stress can be evaluated at the edge of the contact patch such as shown in Figure 11 as points C and E.

We now assume that roadway friction is not sufficient to substantially alter the value of σ_ϕ across the relatively narrow contact patch width, and since the center of the contact patch is flat, then it holds that the value of σ_ϕ at its edge must be constant across the entire contact patch. These membrane stresses are given later in the report as Eqn. (15).

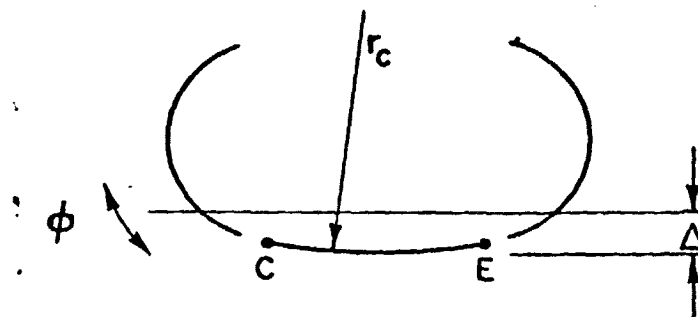


Fig. 11: Cross-section of tire. Points C and E are at edge of contact patch

In addition to these membrane strains, we assume that in region I the carcass becomes completely flat when in contact with the runway surface. This means that the curvature changes undergone by the carcass are exactly equal to the reciprocals of the principal radii of curvature of the tire, namely the values of R of Figure 10 and r_c of Figure 11. Using these values of curvature change and the usual notation for bending strains, along with the moduli of elasticity for a plane orthotropic materials as illustrated in Figure 8, then the additional strain ϵ_θ and the additional stress σ_ϕ due to bending can be gotten and added to the ϵ_θ and the σ_ϕ associated with membrane effects. Note that when running on a test wheel, the drum curvature can be taken into account by defining the curvature change in the θ direction as $(\frac{1}{R} + \frac{2}{D})$, where D is drum diameter.

The equations governing the deformed contact patch are now given by Hooke's law for a plane orthotropic material

$$\epsilon_\theta = \frac{\sigma_\theta}{E_\theta} - \mu_{\theta\phi} \frac{\sigma_\phi}{E_\phi} \quad (3a)$$

$$\epsilon_\phi = \frac{\sigma_\phi}{E_\phi} - \mu_{\phi\theta} \frac{\sigma_\theta}{E_\theta} \quad (3b)$$

where ϵ_θ and σ_ϕ are known. Solving for the other two unknowns gives

$$\sigma_\theta = E_\theta \epsilon_\theta + \frac{E_\theta}{E_\phi} \mu_{\theta\phi} \sigma_\phi \quad (4)$$

and

$$\epsilon_\phi = \frac{\sigma_\phi}{E_\phi} (1 - \mu_{\theta\phi} \mu_{\phi\theta}) - \mu_{\phi\theta} \epsilon_\theta \quad (5)$$

These expressions now give the state of strain in region I.

Using the stress deviator and the strain state, the strain energy stored may now be written as

$$U_{M,B} = \frac{1}{2} \left\{ E_{\theta} \epsilon_{\theta}^2 + \frac{\sigma_{\phi}^2}{E_{\phi}} (1 - \nu_{\phi\theta} \nu_{\theta\phi}) + \sigma_{\phi} \epsilon_{\theta} \left(\frac{E_{\theta}}{E_{\phi}} \nu_{\theta\phi} - \nu_{\phi\theta} \right) \right\} \quad (6)$$

While values of E_{θ} may be obtained readily, the latter two terms of Eqn. (6) contain combinations of elastic constants which are difficult to evaluate. Net theory is of little help here since it predicts that both the terms

$$(1 - \nu_{\phi\theta} \nu_{\theta\phi}) \quad (7a)$$

and

$$\left(\frac{E_{\theta}}{E_{\phi}} \nu_{\theta\phi} - \nu_{\phi\theta} \right) \quad (7b)$$

are zero for inextensible cords. On the other hand, isotropic materials give a value of from 0.75 to nearly 1.0 for Eqn. (7a), but a value of zero for Eqn. (7b).

Lacking better data on cord rubber composites, we must consider values of the constants given by equations (7) to be part of the numerical input data to any computational program.

The other contribution to strain in Section I is associated with the fact that tensile forces in the region of the contact patch change fairly rapidly, thus generating shear stresses in the tire sidewalls associated with equilibrium considerations. This analysis is rather lengthy but leads to contributions which are in the present instance numerically small. In spite of this fact, they are included here since for tires of different geometric construction this effect may be substantial, and would be particularly important in the thermal analysis of tires of radial construction. The details of this analysis are presented in Appendix D, but the resulting strain function is presented here in summary form;

$$U_s = \frac{1}{2} \left[0.857 p_0 \left(1 - \frac{r_f}{r_1} \right) y_s \right]^2 / (h_c^2 G_{\theta\phi}) \quad (8)$$

where the symbols used are defined either in the notation given in the front of this report or in Appendix D.

The net total strain energy change in Region I is now given by the sum of Equations 7 and 8

$$U_I = U_{M,B} + U_s \quad (9)$$

Region II

In Region II the material is tread rubber, which is considered to be isotropic and incompressible. For materials of this type it can be shown that the strain energy may be expressed as

$$U_{II} = G_r \left[\epsilon_{\phi}^2 + \epsilon_{\theta}^2 + \epsilon_y^2 \right] \quad (10)$$

where ϵ_{ϕ} , ϵ_{θ} , ϵ_y are the principal strains and G_r is the trend rubber shear modulus.

The membrane and bending contributions to the strains ϵ_{ϕ} , and ϵ_{θ} are exactly the same as those given in Equations 7 and 8 in the previous section, where now the variable y denotes the distance of a particular computational cell or element above the neutral axis of bending of the section. In addition, the strain ϵ_y must be estimated from considerations of generalized Hooke's law as well as from contact stresses with the runway surface. To a first approximation, the runway contact pressures against the tread surface are close to the inflation pressure of the tire, particularly in the case of aircraft tires where inflation pressure effects are large compared to bending stiffnesses of the carcass. However it is known that the contact pressure distribution in a tire on a flat surface is not uniform. Various experimental measurements have been made on actual tires under running conditions and these generally lead to the conclusion that the

shapes of the contact pressure distributions are approximately parabolic in the circumferential or θ direction, while in the meridional direction, transverse to the direction of rotation, the distributions may range from approximately uniform, to parabolic, to somewhat peaked in the shoulder areas. A numerical study of the influence of these various shapes on the strain energy stored in the elements in compression is carried out in Appendix E, where it is shown that to a first approximation a good numerical estimate of the influence of contact pressure on strain in the tread elements is given by:

$$\epsilon_y = - \frac{1.5p_o}{E_r} \quad (11)$$

where E_r is the trend rubber modulus and p_o is the inflation pressure. Combining Equation 10 with a generalized Hooke's law gives the total strain in a direction perpendicular to the carcass midline as Equation 11:

$$\epsilon_y = - \frac{1.5p_o}{E_r} - 0.5(\epsilon_\phi + \epsilon_\theta) \quad (12)$$

where again ϵ_ϕ and ϵ_θ contain the membrane contributions from the carcass structure plus the bending contributions. Equations 11 and 12 may now be combined into Equation 10 in order to form the total strain energy per unit volume associated with Region II of the tire.

Region III

In Region III of the tire we again consider the principal strains in the ϕ and θ directions, but in this case there is no contact with the runway surface and strains in the direction perpendicular to the midplane are neglected. We include both membrane and bending effects in the calculation of the total

strain on each computational cell or element. The bending strain in the ϕ direction may be obtained from geometric considerations directly, since it arises from changes in radius of curvature which can be computed using the circular arc model discussed in Appendix A and illustrated in Figures 3 and 5. Bending strains in the θ direction are considered negligible in this region.

The membrane strain in the circumferential direction θ is taken in this case directly from considerations of axisymmetric deformation of the tire. It is seen that as the tire passes from point A to point B of Figure 2, the radial dimension of a material point j in Figure 5 changes from z_i to z_f . This allows calculation of the membrane strain for an axisymmetric deformation pattern, as given by Eqn. 13.

$$\epsilon_{\theta} = \frac{z_f - z_i}{z_i} \quad (13)$$

The membrane stresses in the tire sidewall must be used to obtain the strains in the ϕ direction. This is so because we have no ready geometric model for estimating these from the tire shape changes as illustrated in Figure 3. Referring to Figure 3, it may be shown from equilibrium considerations that the change in membrane stress in the ϕ direction between Figures 3a and 3b may be written as

$$\sigma_{\phi} = \frac{p_o}{2h_c} \left[r_f \left(1 + \frac{h_f}{z_f} \right) - r_i \left(1 + \frac{b_i}{z_i} \right) \right] \quad (14)$$

Since the strains in the θ direction are known, Eqn. (13) and the stresses in the ϕ direction, Eqn. (14), then Hooke's law must be used to obtain either the stress in the θ direction or the strain in the ϕ direction. Again assuming orthotropic properties for the sidewall structure, and solving for the strain in the ϕ direction gives once more, as in Eqn. (5).

$$\epsilon_{\phi} = \frac{\sigma_{\phi}}{E_{\phi}}(1 - \mu_{\theta\phi}\mu_{\phi\theta}) - \mu_{\phi\theta}\epsilon_{\theta} \quad (15)$$

This leads to the same expression for strain energy as was found previously for Region I,

$$U_{M,B} = \frac{1}{2} \left\{ E_{\theta} \epsilon_{\theta}^2 + \frac{\sigma_{\phi}^2}{E_{\phi}}(1 - \mu_{\phi\theta}\mu_{\theta\phi}) + \sigma_{\phi} \epsilon_{\theta} \left(\frac{E_{\theta}}{E_{\phi}} \mu_{\theta\phi} - \mu_{\phi\theta} \right) \right\} \quad (16)$$

In addition, the shear stresses caused by variation in membrane forces previously discussed as Eqn. 7 also appear in the sidewall in Region III. The expression for these is exactly the same as Eqn. 7, and will not be repeated here. However, using this term, the total strain energy change per unit volume in Region III may be obtained by summing Eqn. 16 and Eqn. 7 to give:

$$U_{III} = U_{M,B} + U_s \quad (17)$$

This implies that all of the shear forces generated by the variation of membrane stresses are carried by the carcass region of the tire, Region III, and none by the sidewall rubber denoted as Region IV.

Region IV

In Region IV of the tire we again deal with a rubber covering but in this case one which does not contact the runway surface. The material is assumed to be isotropic and incompressible. The same considerations apply here as applied in Region II except that the strain perpendicular to the carcass midline is neglected in this case. The modulus of this rubber covering is low enough so that it is extremely compliant as compared with the sidewall carcass structure. For this reason it is assumed that it will take on the same membrane strains as the sidewall carcass region III, and will only vary from it due to bending effects caused by its

further distance away from the neutral axis of bending. For this reason the very same expressions used for the calculation of the bending and membrane strains in Region III are also valid here. Specifically, these are Eqns. 13 and 14, and using them the strain energy change per unit volume in this region may also be expressed in a fashion similar to that of Eqn. (10), again because of the fact that the ϕ and θ directions are principal directions. This is given by Equation 18.

$$U_{IV} = G_r \left[\epsilon_{\phi}^2 + \epsilon_{\theta}^2 \right] \quad (18)$$

where ϵ_{ϕ} is given by Eqn. 15 and ϵ_{θ} by Eqn. 14, using the appropriate values of the variable y to denote the distance of the specific computational cell or element from the neutral axis of bending, and further using the appropriate dimension z in Eqn. 13 for the same cell.

Region V

In this region we consider the bead elements themselves as components which lose energy during cyclic stressing of the tire. An analysis of this is given in Appendix B, and the result of that analysis may be used to introduce a total or gross strain energy change in each bead of the tire. Using the expressions derived in Appendix B, this becomes

$$U_V = \frac{1}{2} (T_{Rf} - T_{Ri})^2 / (A_B^2 E_B) \quad (19)$$

HEAT GENERATION RATES

For purposes of obtaining heat generation rates from strain energy stored during elastic cycling of the tire we utilize the conventional Kelvin-Voigt mechanical model of an elastic solid which exhibits loss characteristics under cyclic stress. Referring to Figure 1, we see that it can represent experimental data observed on many materials, including the polymeric materials used in aircraft tires such as rubber, nylon in textile cord form and even the bead wire assembly, provided that the loss characteristics are measured properly. One widely accepted method of representing such a phenomena as the Kelvin-Voigt model, is illustrated in Figure 12 using the conventional spring and dashpot notation.

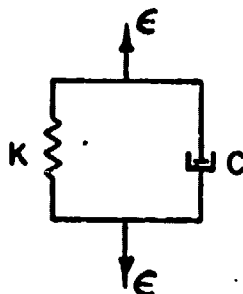


Fig. 12: Spring-dashpot model of a material exhibiting loss

We impose on Figure 12 a cyclic sinusoidal strain in the form

$$\epsilon = \epsilon_0 \sin \omega t \quad (20)$$

The stress necessary to maintain such a sinusoidal strain is given by

$$\sigma = K\epsilon + C\dot{\epsilon} = K\epsilon_0 \sin \omega t + C\omega\epsilon_0 \cos \omega t \quad (21)$$

It is customary to convert this representation of Eqn. 21 into a form using the elastic constants E' and E'' , representing the characteristics of a material exhibiting loss, in the form of Eqn. 22.

$$\sigma = E'\epsilon_0 \sin \omega t + E''\epsilon_0 \cos \omega t \quad (22)$$

It is clear from that representation that both E' and E'' may be functions of frequency and usually are. In addition, particularly in polymeric materials, they show marked dependence on temperature and of course material composition.

The energy loss during one cycle of stress is given by

$$\text{Energy Loss} = W = \int_{\text{cycle}} \sigma d\epsilon = \pi E'' \epsilon_0^2 \quad (23)$$

We define the ratio of E'' to E' as a material property called $\tan \delta$ as given by Equation 24.

$$E''/E' = \tan \delta \quad (24)$$

Combining Equation 23 and 24 gives

$$W = E'\epsilon_0^2 \tan \delta = \pi U \tan \delta \quad (25)$$

where U is the elastic strain energy stored during the cyclic stressing process. This is the form in which energy loss is commonly expressed, using the elastic constants E' and E'' directly obtained from experimental data, or alternately using $\tan \delta$ directly obtained from measurement. Several instruments are commercially available for the measurement of loss properties such as $\tan \delta$, and values of $\tan \delta$ are commonly available for many polymeric materials.

The materials used in tire construction exhibit properties which are close to being incompressible. For that reason it is assumed that the hydrostatic component of stress results in no elastic energy storage in a typical element of material, and hence exhibits no loss during the cyclic stressing process. Using this assumption, it may be shown that there are no effects of pre-stress on the energy loss per stress cycle, and for that reason Figure 1

of this report, showing the cyclic stress process between two general points, is drawn independent of the pre-stress level in the tire. In other words, we begin the strain measuring process from the inflated state of the tire and only consider that energy storage which occurs in a material element as it moves from the inflated but unloaded state to a position which lies directly in the center of the contact patch of the loaded region. The units of Eqn. 25 are the same as those of strain energy, namely work per unit volume. These must be converted to a rate of heat generation per unit volume in order to be used in the general heat diffusion equation discussed in the subsequent sections. Since aircraft velocities are commonly expressed in English units of feet per second, $\tan\delta$ is dimensionless, and the tire diameter may conveniently be expressed in inches, and using the elastic strain energy in inch/pound units, then one may write:

$$\begin{aligned}
 U/12 &= \frac{\text{ft. lbs. energy}}{\text{cu. in. volume}} / \text{stress cycle} \\
 &\times \frac{1}{778} \text{ BTU/in}^3 / \text{cycle} \\
 &\times 252 \text{ cal/in}^3 / \text{cycle} \\
 &\times \frac{1}{(2.54)^3} \text{ cal/cm}^3 / \text{cycle}
 \end{aligned}$$

But $\frac{r_r \omega}{12} = v_o$ where v_o = aircraft velocity, fps

$$r_r = \text{rolling radius of tire, inches}$$

$$r_r = r_o - \Delta/3$$

$$\omega = \text{rad/sec}$$

$$= \frac{12v_o}{(r_o - \Delta/3)} \times \frac{1}{2\pi} \text{ cycles/sec.}$$

$$\text{Loss/cycle} = W = \pi U \tan\delta$$

Heat generation rate in cal/cm³/sec =

$$\begin{aligned} \dot{q} &= U \times \frac{1}{12} \times \frac{252}{778} \times \left(\frac{1}{2.54}\right)^3 \times \frac{12}{2\pi} \times \frac{v_o}{(r_o - \Delta/3)} \times \pi \tan \delta \\ &= .00988 \frac{U v_o \tan \delta}{(r_o - \Delta/3)} \approx 0.01 \frac{U v_o \tan \delta}{(r_o - \Delta/3)} \end{aligned} \quad (26)$$

where r_o = outside radius of tire, inches.

Δ = tire deflection, inches

v_o = aircraft velocity, feet/second

U = elastic energy, inch-pounds/cubic inch.

TEMPERATURE DISTRIBUTION MODEL

Referring first to Figure 9, the tire must be divided into segments or cells in each of which the rate of heat generation is considered constant, and in which temperature will be calculated on the basis of being averaged across the cell area. In assigning the geometric location of cells such as illustrated in Figure 9, we attempt to maintain material constancy across each cell, in the sense that the interface between the pure rubber region and the carcass region is used as a dividing line for a series of cells as well. This allows the properties of each cell to be essentially uniform, which is a considerable convenience in subsequent calculations. The stress state in each cell is calculated on the basis of the centroid of each cell area, and is considered to be averaged across the cell volume. The geometric location of the cell is taken to be the coordinates of the cell centroidal area such as shown in Figure 13.

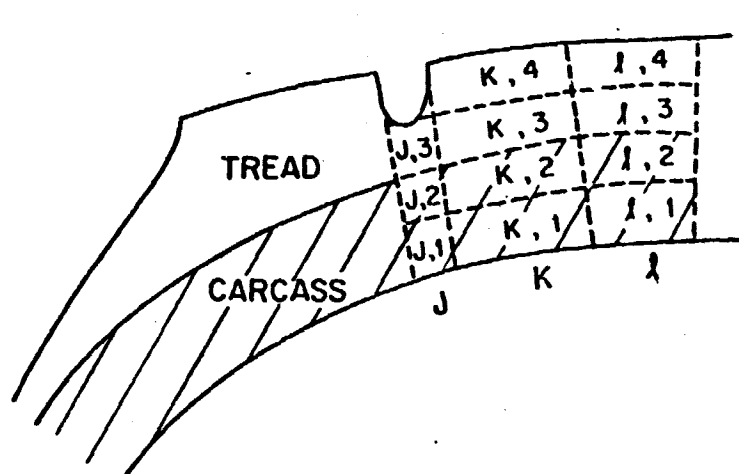


Fig. 13: Distribution of computational elements in the tread region

We have consistently utilized quadralateral elements in constructing the numerical analog to this solution. Thus each element either loses or gains heat from four faces, and this may be through conduction when the element in question is bounded by a similar element or it may be by convection from a surface face, or it may be by conduction to either the flange of the wheel or to the runway surface for those special elements which come in contact with them.

For purposes of conduction to the wheel flange, a similar set of elements to those shown in Figure 13 must be laid out on the wheel flange using the appropriate thermal characteristics of the wheel material, so that heat flow can take place by direct conduction between the bead area of the tire and the flange. There will inevitably be a certain contact resistance between the bead seat and the flange material, but this factor is as yet unknown and is neglected in the subsequent computations.

Contact with the runway surface is more difficult to quantify since it occurs only periodically. To a first approximation we treat that process in a similar fashion using the thermal conductivity of the runway material, but allowing only that fraction of the conduction process to occur as is proportional to the time spent by each surface element in contact with the runway. The remaining part of the cycle is occupied by those tread surface elements which contacted the runway surface now freely moving in the atmosphere, and during that fraction of the cycle the normal convection process from the surface occurs.

Using the well known expression for diffusion of heat in a solid body under conditions of internal heat generation, such as given by Carslaw and Jaeger [1], the equation for conduction of heat for a typical element is given by Eqn. 27.

$$KV^2\theta = \rho \frac{\partial \theta}{\partial t} - q \quad (27)$$

This may be written for finite difference purposes in the form

$$\frac{\Delta\theta}{\Delta t} = \dot{q} + \bar{\alpha}_{K-1,K,\ell}(\theta_{K-1,\ell} - \theta_{K,\ell}) + \bar{\alpha}_{K,K+1,\ell}(\theta_{K+1,\ell} - \theta_{K,\ell}) \\ + \bar{\alpha}_{K,\ell-1,\ell}(\theta_{K,\ell-1} - \theta_{K,\ell}) + \bar{\alpha}_{K,\ell,\ell+1}(\theta_{K,\ell+1} - \theta_{K,\ell})$$

where the elements used in Eqn. (28) are illustrated in Fig. 14;
and where

$$\bar{\alpha}_{m,n} = \frac{KA}{d}$$

with

- K = thermal conductivity
- A = area of contact between subscripted elements
- d = distance between centroids of subscripted elements

	K, $\ell-1$	
K-1, ℓ	K, ℓ	K+1, ℓ
	K, $\ell+1$	

Fig. 14: Notation for thermal elements

The basic method of computation is to use small time increments and to calculate the temperature rise in each cell utilizing the temperatures of adjoining elements from the previous time increment computation. There are several factors which make this type of computation possible. First of all, it is well known in heat transfer calculations that if the quantity given by Equation 29 is large, then stability of such a time based forward computation is assured and convergence to correct results will be obtained. For that reason we have chosen to keep cell elements moderately large and time increments small since this reduces requirements for computer memory, and also insures stability of the computation.

$$M = \frac{\Delta x^2}{a \Delta t} \quad (29)$$

where

$$a = \dot{q}/\alpha$$

$$\Delta x = \text{element size}$$

$$\Delta t = \text{time increment}$$

Secondly, we are dealing here with a type of computation where the dominant term is the rate of heat generation \dot{q} , and for purposes for aircraft taxi and take-off the heat build up occurs over a relatively short period of time, so that the heat generation term almost completely controls the temperature rise in the tire. Heat diffusion, at least for the take-off case, is a minimal effect. This means that heat conduction using adjoining cell temperatures from the previous time interval incur only very small errors in the final temperature distribution in the tire.

The heat transfer coefficients from tire to air are not particularly well known in this case, but again it is fortunate that taxi take-off cycles are relatively short, so that again the rate of internal heat generation is the dominant term. However,

in studying taxi and combined taxi take-off operations, more emphasis is placed on the accuracy of the heat transfer and heat conduction coefficients associated with this problem. In that case those coefficients become more important. The numerical proportioning of the heat transfer coefficients is given in detail in Appendix H.

The method of temperature computation using Eqn. 27 now consists of starting from whatever initial temperature state one wishes in each of the cells, allowing a short time interval to take place and computing the heat generated in each cell using the concepts developed in the previous two sections. In carrying out such computations a knowledge of the material loss characteristic $\tan\delta$ must be known, and these are given in the last section of this report.

At the end of the first time interval the temperature field in the entire tire is calculated and is used as a basis for the heat transfer characteristics during the second time interval, which follows immediately. The computation is sequential, thus requiring minimum memory storage in a computer, and may conveniently be carried out on relatively unsophisticated equipment such as microcomputers or minicomputers.

The contained air temperature in the tire is often measured and used as an indication of overall tire heating. It's calculation requires a separate analysis given in Appendix H. From this analysis, the contained air temperature is shown to lag behind the inner surface temperature of the tire. In the initial stages of tire heating, its value is given by

$$\Delta y = \beta \Delta t (\theta - y)$$

where

- y = contained air temperature
- θ = weighted average of tire inner surface temperatures
- Δt = time increment
- β = a constant involving properties of the air and heat transfer coefficients.

The heat transfer coefficients chosen for the inner surface are presently based on the concepts that inner peristaltic pumping velocities are small, just sufficient to insure good mixing. This is an area where more measurements are needed.

EXPERIMENTAL PROGRAM

The problem in hand is an extremely complex one and could not be expected to be verified without considerable experimental data. A number of assumptions are used in the computation of the rate of internal heat generation in the tire, and many of these assumptions can only be verified by direct measurement of temperature fields in actual tires. For that reason a comprehensive experimental program was carried out by the Impact Dynamics Branch, Langley Research Center, National Aeronautics and Space Administration, Hampton, Virginia. Most of the work was done at their Wallops Island Test Station, using a specially designed truck with a yoke and loading apparatus designed for the testing of tires.

Thermocouples were installed at the University of Michigan in approximately twenty 22 x 5.5 8-ply and 12-ply rated aircraft tires furnished by NASA Langley. Most of these thermocouple installations were achieved by implanting appropriate thermocouples in holes drilled in the tire carcasses after having been buffed but prior to retreading. Subsequently the tires were retreaded by a commercial retreader, and were wired for internal temperature measurements during both straight line rolling, cornering and braking. For purposes of this report only the straight line rolling data will be used. Due to load limitations of the test equipment the full rated loads of the tires could not be applied, and since it was desired to achieve normal tire deflections, inflation pressures were also kept below normal values.

The tire temperature data obtained from typical test runs is presented in the next section of this report where it is compared with computation. In general the use of appropriate thermocouples carefully implanted in the tire was sufficient to give a good picture of the internal temperature distribution. A thorough summary of this information has been presented in a separate NASA document.

Due to limited load and pressure combinations which could be used on the NASA equipment, the University of Michigan conducted

a short series of taxi-takeoff roll tests on instrumented tires of the same size at Wright-Patterson Air Force Base, Dayton, Ohio, using their 120 inch aircraft tire dynamometer. With this equipment full rated loads and speeds could be obtained. This data is also presented in the subsequent section where it is compared with experiments, and this represents a different set of temperature rise values since it involves loads, pressures and speeds which are consistent with real operating conditions.

Referring to earlier sections of the report, it is clear that the rate of heat generation depends on the strain energy stored in the tire, which in turn depends both on bending and membrane effects. While deflection itself controls the bending contribution to this problem, the membrane contribution is clearly dependent on the inflation and thus both effects are needed to give a realistic description of tire temperature rise during service conditions.

While a great deal of temperature data was obtained by these two series of test programs, it is so voluminous that only selected parts of it have been used for purposes of comparison with calculation in this report. In order to provide a complete record of the test data available, however, Table 1 shows the load and speed combinations available in straight line rolling from the NASA Wallops Island tests, while Table 2 shows the load, pressure and speed combinations available from the University of Michigan tests carried out at Wright-Patterson Air Force Base. Some of this data will now be extracted in detail and used in a subsequent section of this report for comparison with calculation.

Table 1
Operating Conditions NASA Wallops Island Tests

	Load lb	Pressure psi	Speed MPH
<u>NASA</u> <u>8PR</u>	2700	83	20
	3270	83	20
	4000	83	20
	4000	115	20
	4000	150	20
<u>NASA</u> <u>12PR</u>	2560	55	20
	3150	55	20
	4000	55	20
	4000	110	20
	4000	78	20
	4000	78	35
	4000	78	50

Table 2
Operating Conditions - University of Michigan Tests

	Load lb.	Pressure psi	Speed MPH
<u>UM</u> <u>8PR</u>	4350	125	20
	3263	87	20
	4350	156	20
	4350	94	20
<u>UM</u> <u>12PR</u>	7100	209	20
	5325	132	20
	7100	261	20

CALCULATION VS. EXPERIMENT

We now desire to compare calculation of temperature distribution in the tire with data measured from both NASA Wallops Island tests and the University of Michigan tests. In order to carry out the computations the material characteristics must be assigned. For this purpose we use data estimated from the literature for the material characteristics of the tire as given in Table 3.

Using a time increment, as defined in Eqn. 28, of $t = 10$ seconds, and using the material characteristics and tire geometries for both the 8PR and 12PR 22 x 5.5 tires, as determined in Appendix H, computation was carried out over short time intervals for the temperature rise in these tires under conditions experienced by both the Wallops Island tests and the tests conducted by the University of Michigan. Comparison between calculation and experiment is shown in Figures 15 through 33, where the experimental data is plotted as a function of time. The computations are carried out using Eqn. 28 and the material constants given in Table 3, along with the specific geometry for these tires, as defined in Appendix H.

It should be emphasized that while the outside dimensions of these two ply-rating tires are the same, their internal characteristics are quite different and the modeling is completely different. The elements representing the heat transfer cells are not the same, nor is the nature and extent of the carcass area. The 8PR version of the tire has only one bead, while the 12PR version has two beads. For these reasons the two sets of comparisons should be considered as being taken on two separate tires.

As can be seen from these figures, the calculations generally agree well with the experimental data. In particular they predict the ranking of hottest areas in the tire at a particular location, i.e. from outside to inside and vice-versa. They support the reversal of inside-outside temperature gradient between sidewall and tread, a phenomenon observed experimentally. In addition they generally support the experimental data observed over a rather wide range of inflation pressures and tire deflections.

Element	E	G	$\tan\delta_0$ (5)	α	K(3) (4)	ρ (3)	C_p (3)
Tread(II)	(1)	335	0.2	-	5×10^{-4}	1.0	0.5
Carcass (I,III)			0.1	(2)	5×10^{-4}	1.0	0.5
Sidewall Rubber (IV)	15×10^6	335	0.15			1.0	0.5
Bead (V)			0.03				

Material Characteristics

Table 3

* See Fig. 7

(1) See Appendix C. Use $G = 335$.

(2) Calculated by cosine law using $\alpha = 35^\circ$ crown angle

(3) See Appendix H

(4) $\text{cal-cm}/^\circ\text{C-cm}^2\text{-sec}$

(5) Values of $\tan\delta_0$ are given for 25°C . For higher temperatures, $\tan\delta$ is calculated by an approximate expression

$$\tan\delta = \tan\delta_0 \cdot e^{-.01\Delta\theta}$$

where $\Delta\theta$ is the temperature rise in $^\circ\text{C}$ above ambient.

From a study of the comparisons between these computations and the experimental data it is concluded that the major trends in the temperature rise problem can be calculated adequately for relatively short term taxi-takeoff conditions. More emphasis must be placed on obtaining good thermal properties of the materials and better heat transfer coefficients before we can hope to achieve success in calculating long term or near equilibrium temperature conditions in the tire.

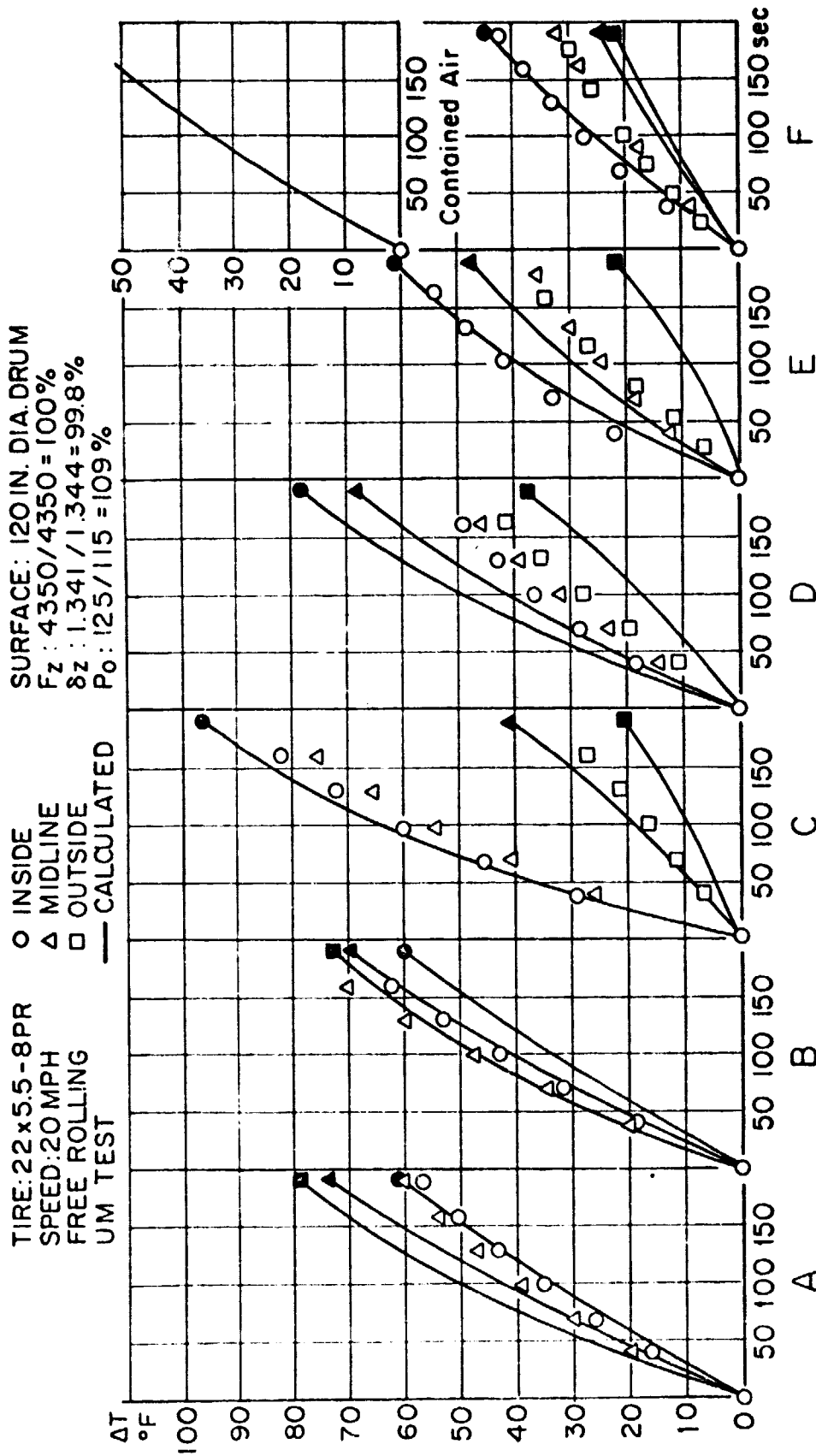


Fig. 15: Measured and Calibrated Tire Temperature Profiles.

SURFACE: 120 IN. DIA. DRUM
Fz: 3260/4350 = 75%
Sz: 1.332/1.344 = 99%
Po: 87/115 = 76%

○ INSIDE
 △ MIDLINE
 □ OUTSIDE
 — CALCULATED

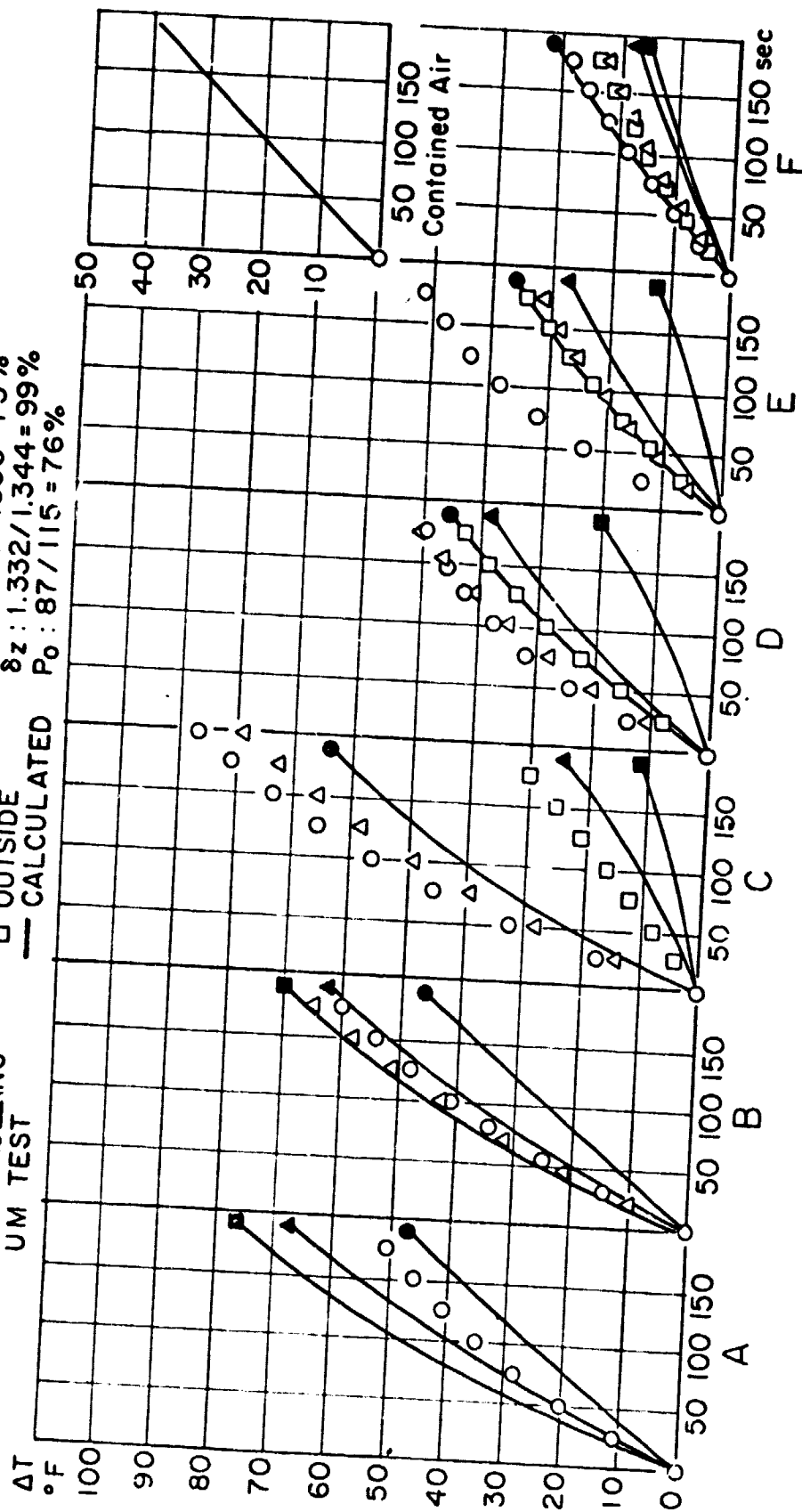


Fig. 16: Measured and Calibrated Tire Temperature Profiles.

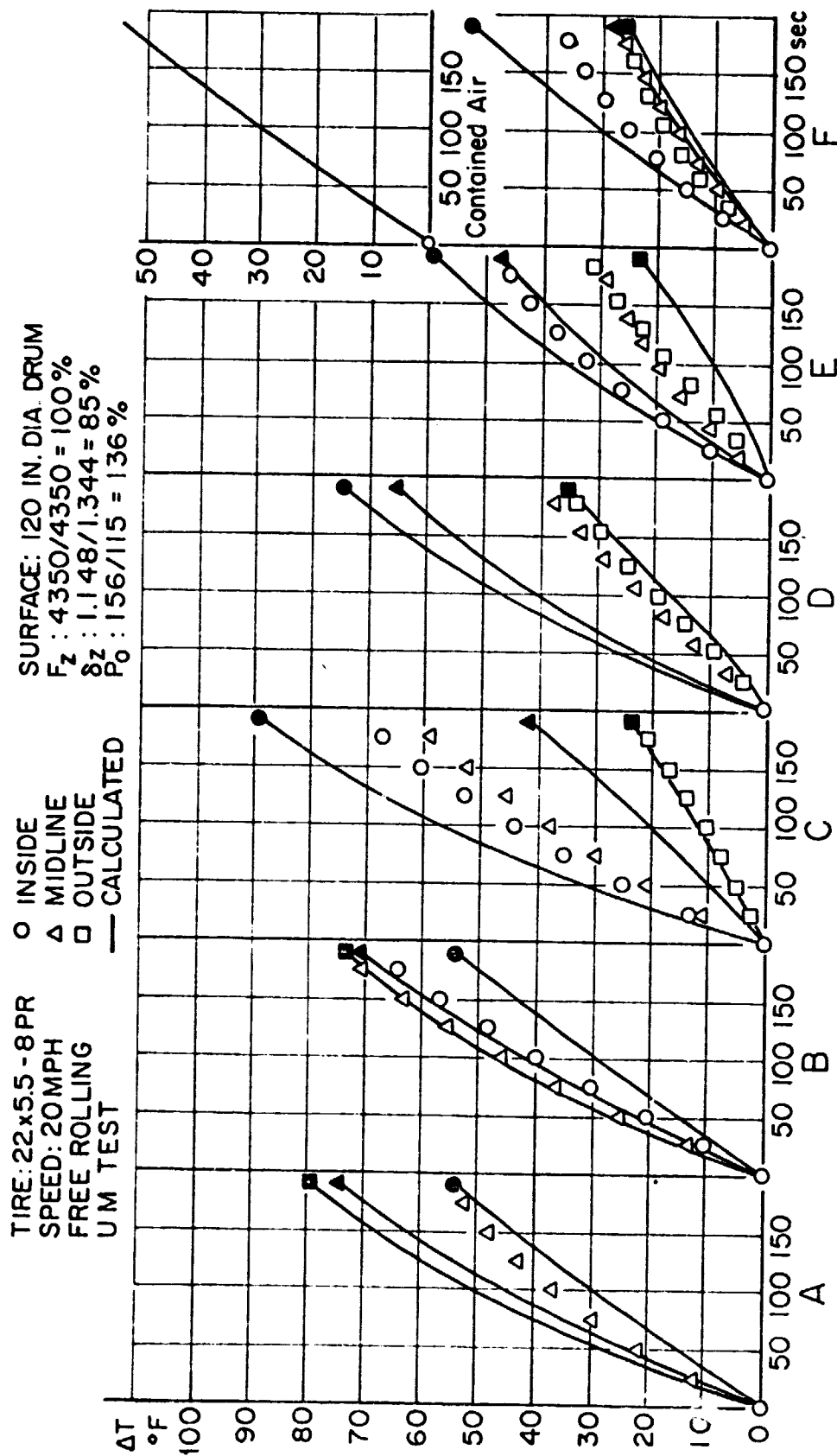


Fig. 17: Measured and Calibrated Tire Temperature Profiles.

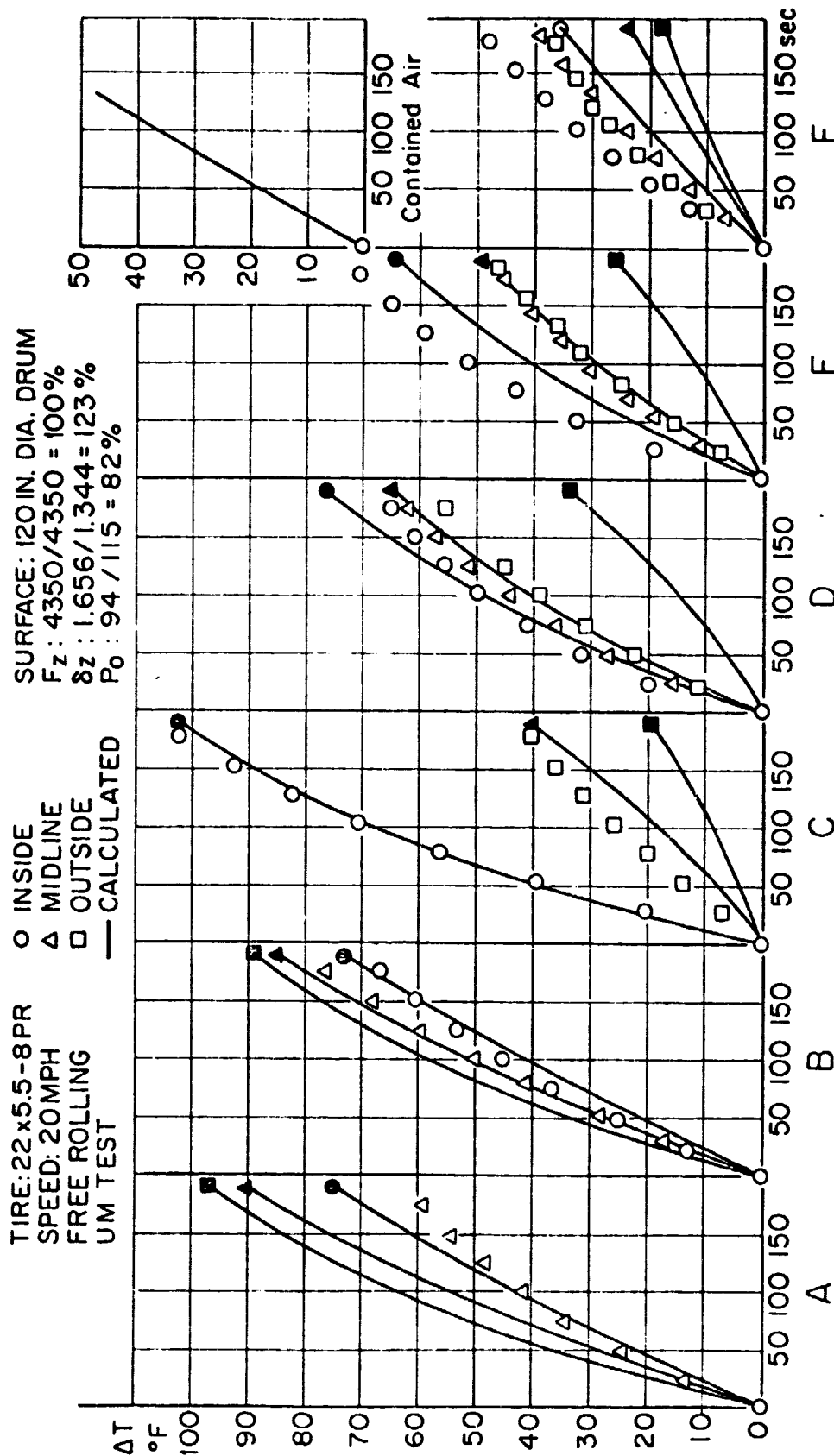


Fig. 18: Measured and Calibrated Tire Temperature Profiles.

TIRE: 22x5.5 8 PR
SPEED: 20MPH
FREE ROLLING
NASA TEST

○ INSIDE
△ MIDLINE
□ OUTSIDE
— CALCULATED

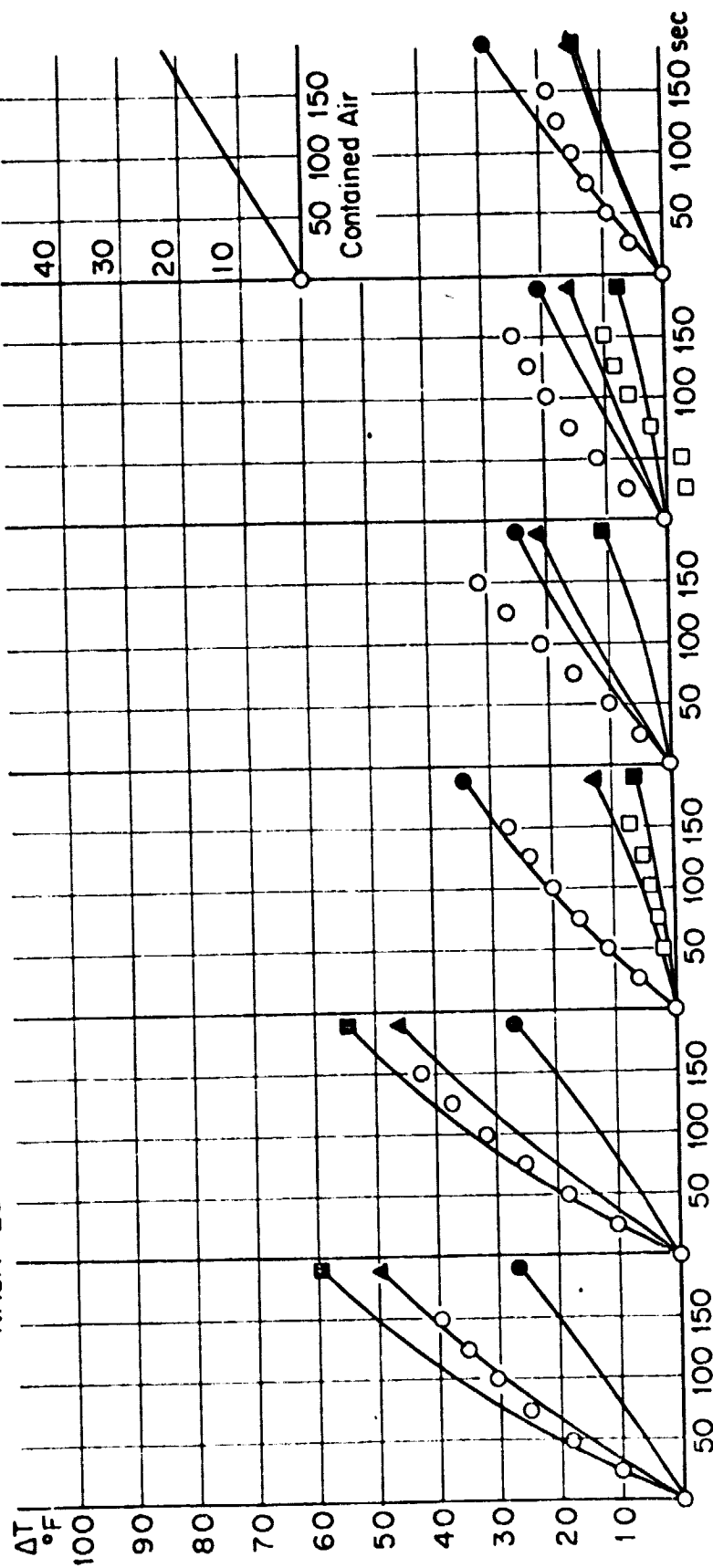


Fig. 19: Measured and Calibrated Tire Temperature Profiles.

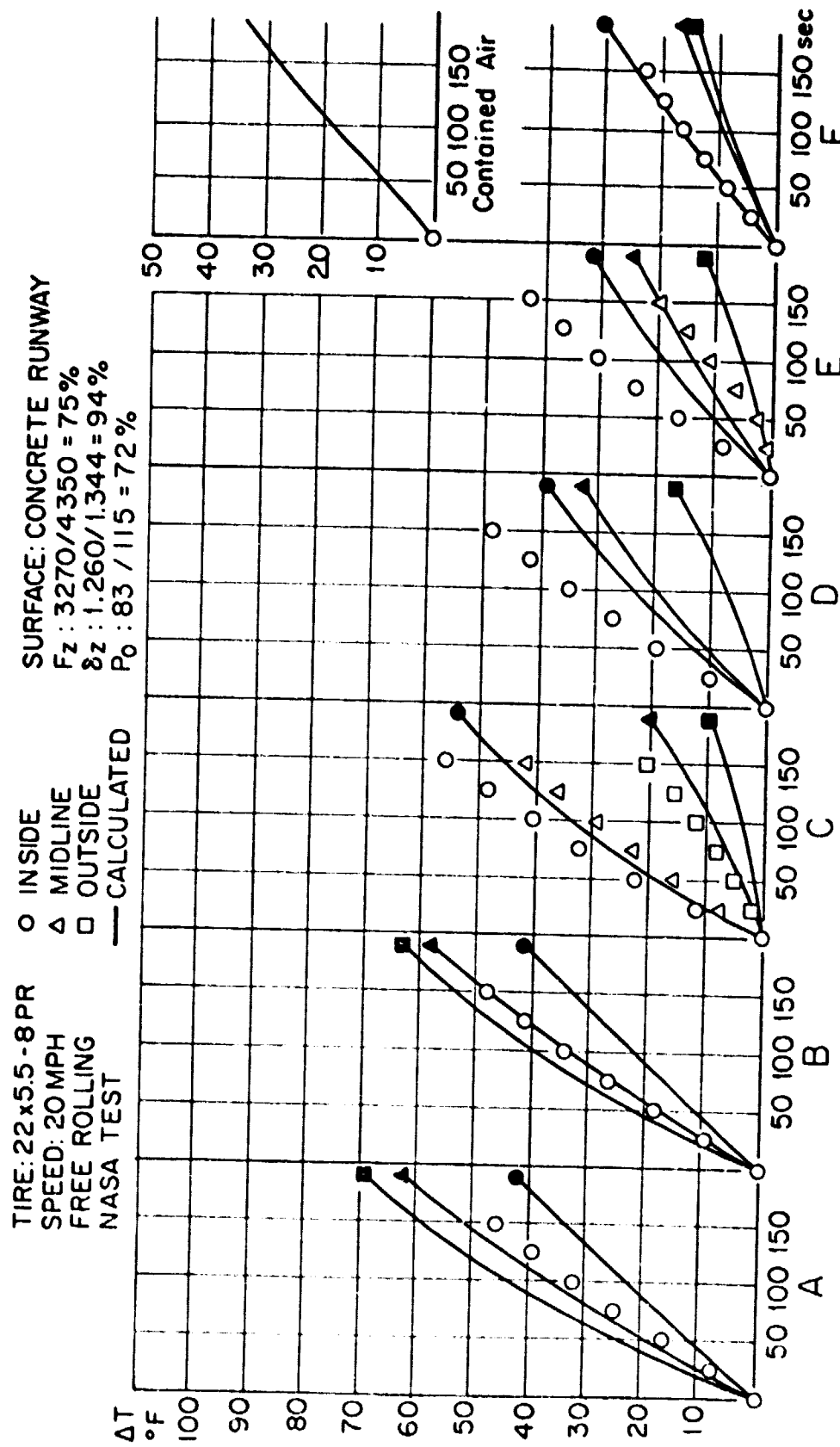


Fig. 20: Measured and Calibrated Tire Temperature Profiles.

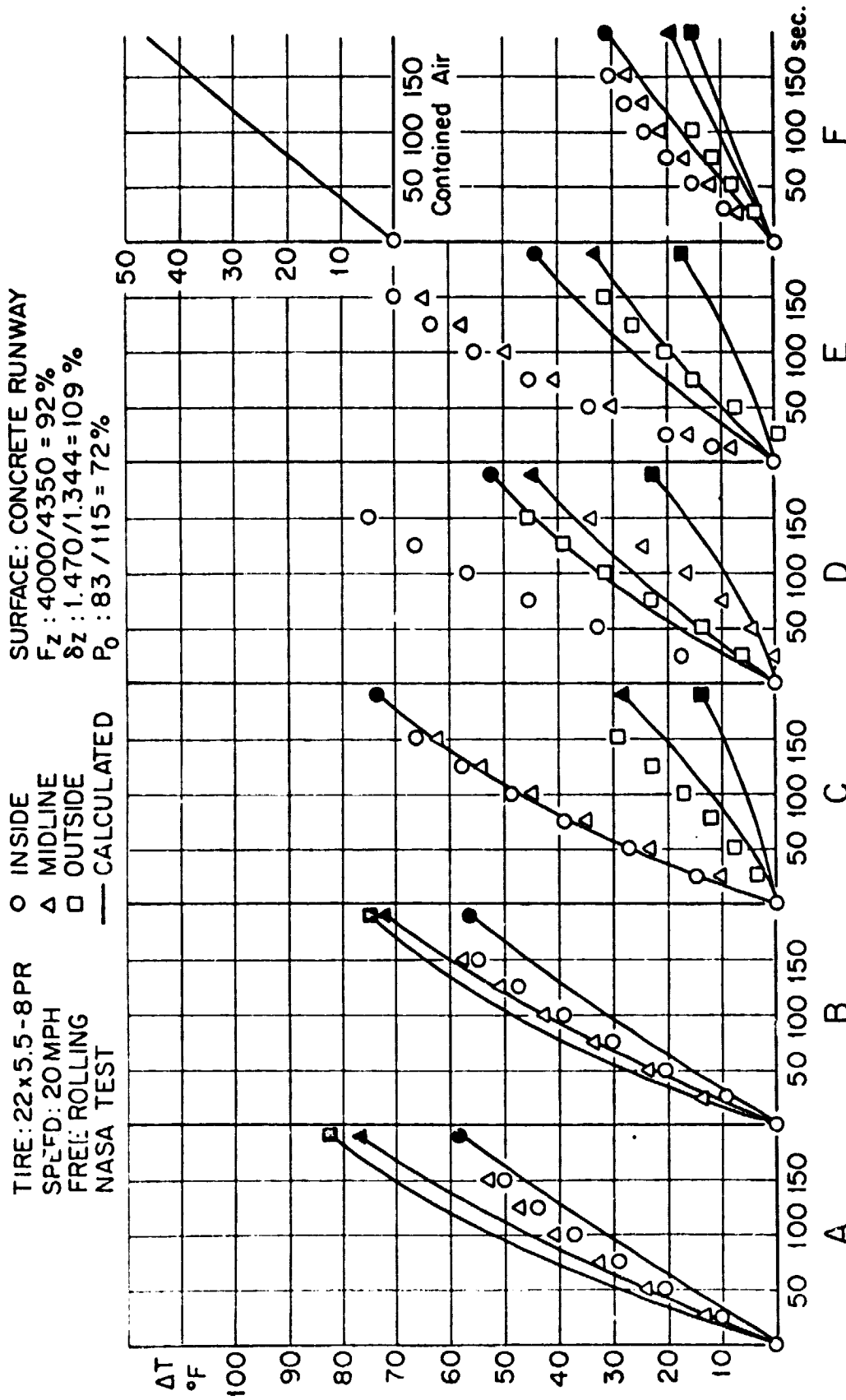


Fig. 21: Measured and Calibrated Tire Temperature Profiles.

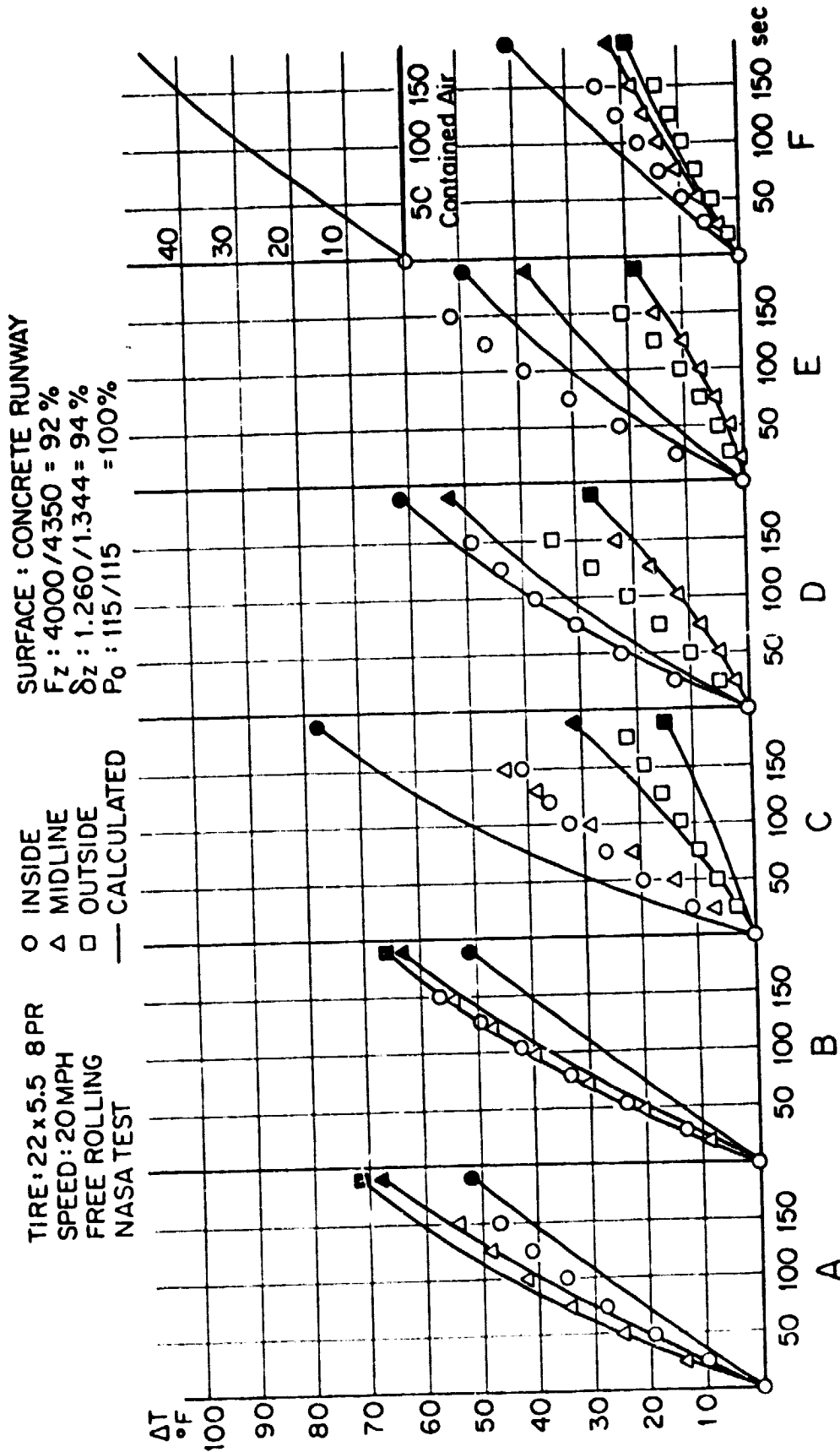


Fig. 22: Measured and Calibrated Tire Temperature Profiles.

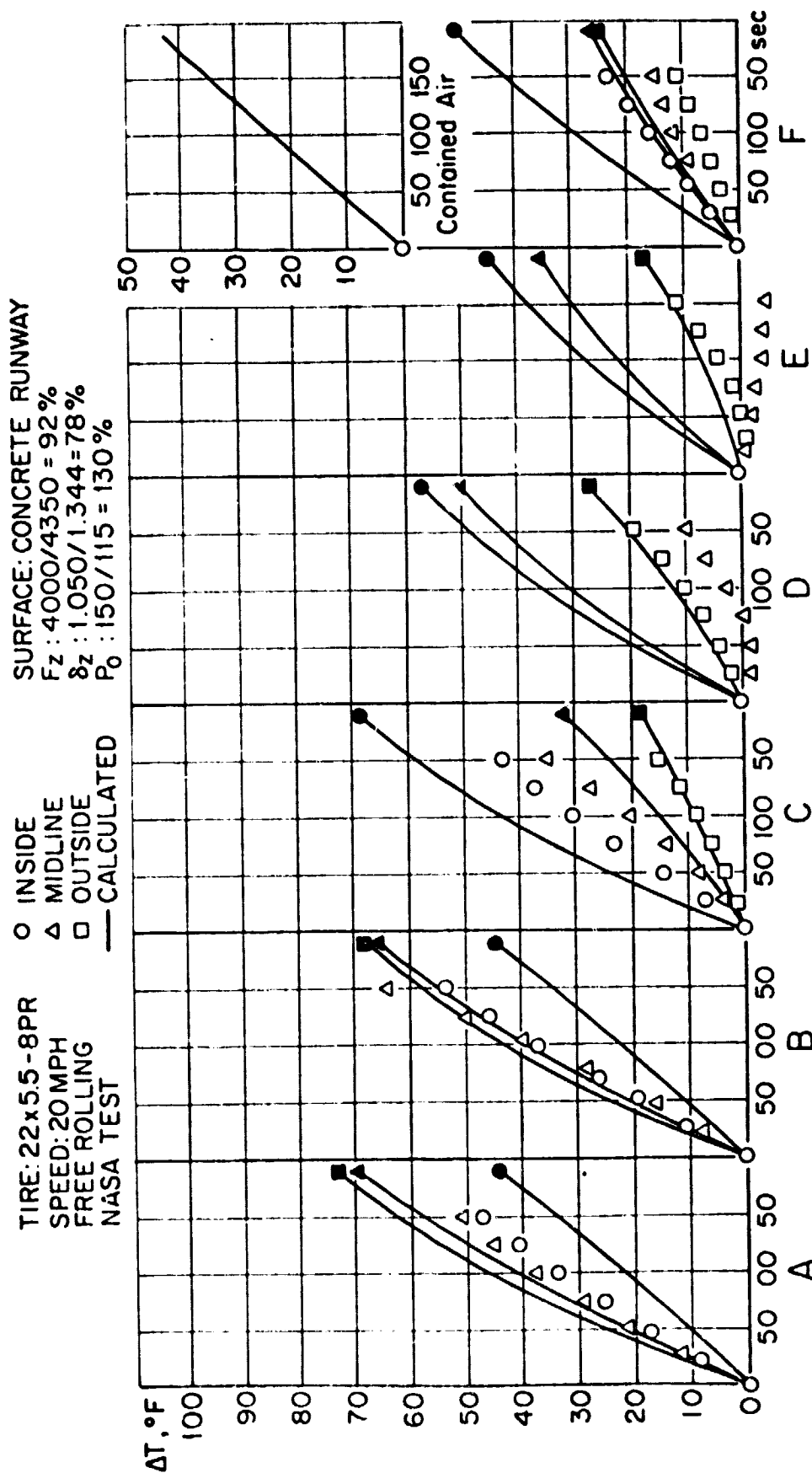


Fig. 23: Measured and Calibrated Tire Temperature Profiles.

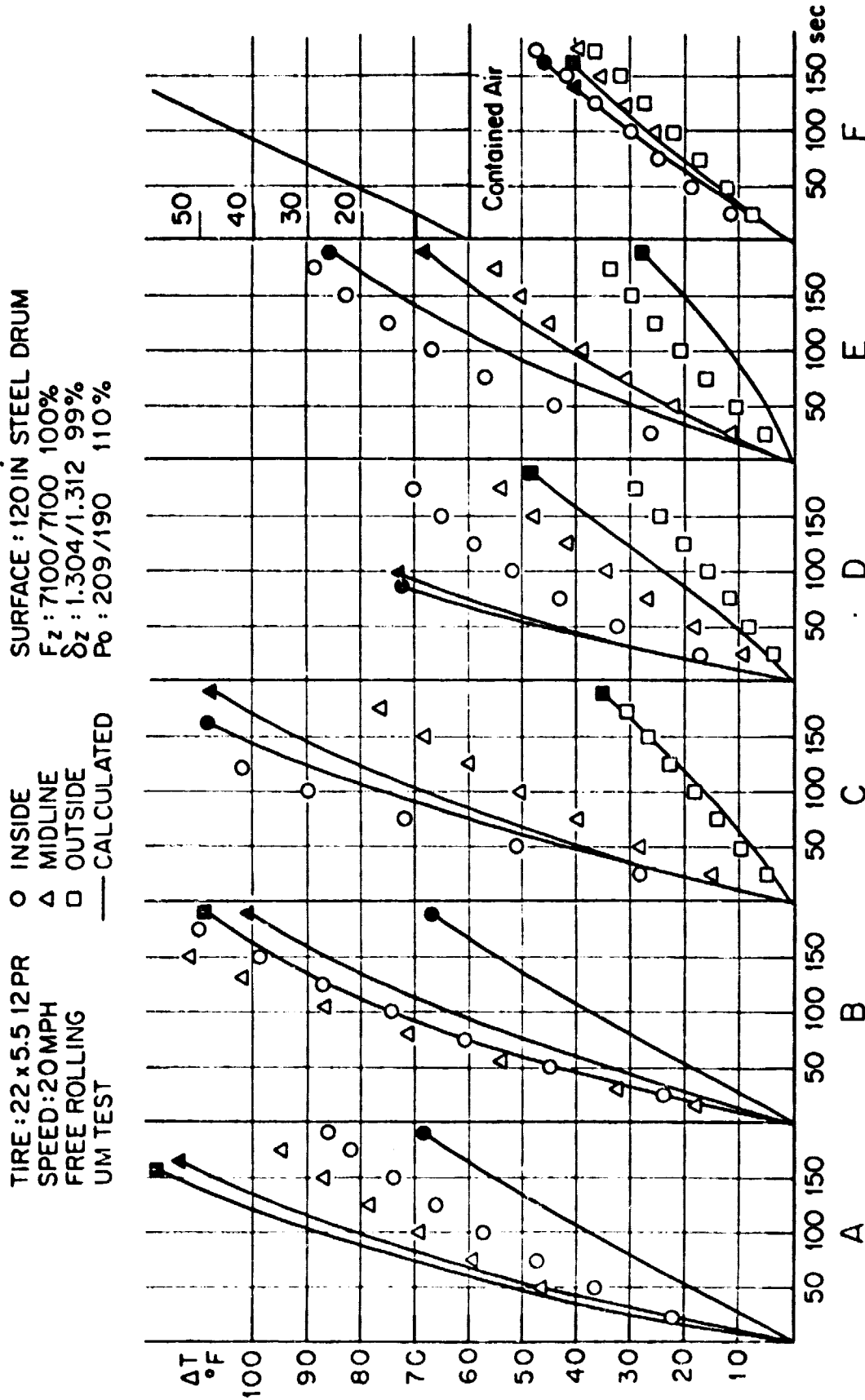


Fig. 24: Measured and Calibrated Tire Temperature Profiles.

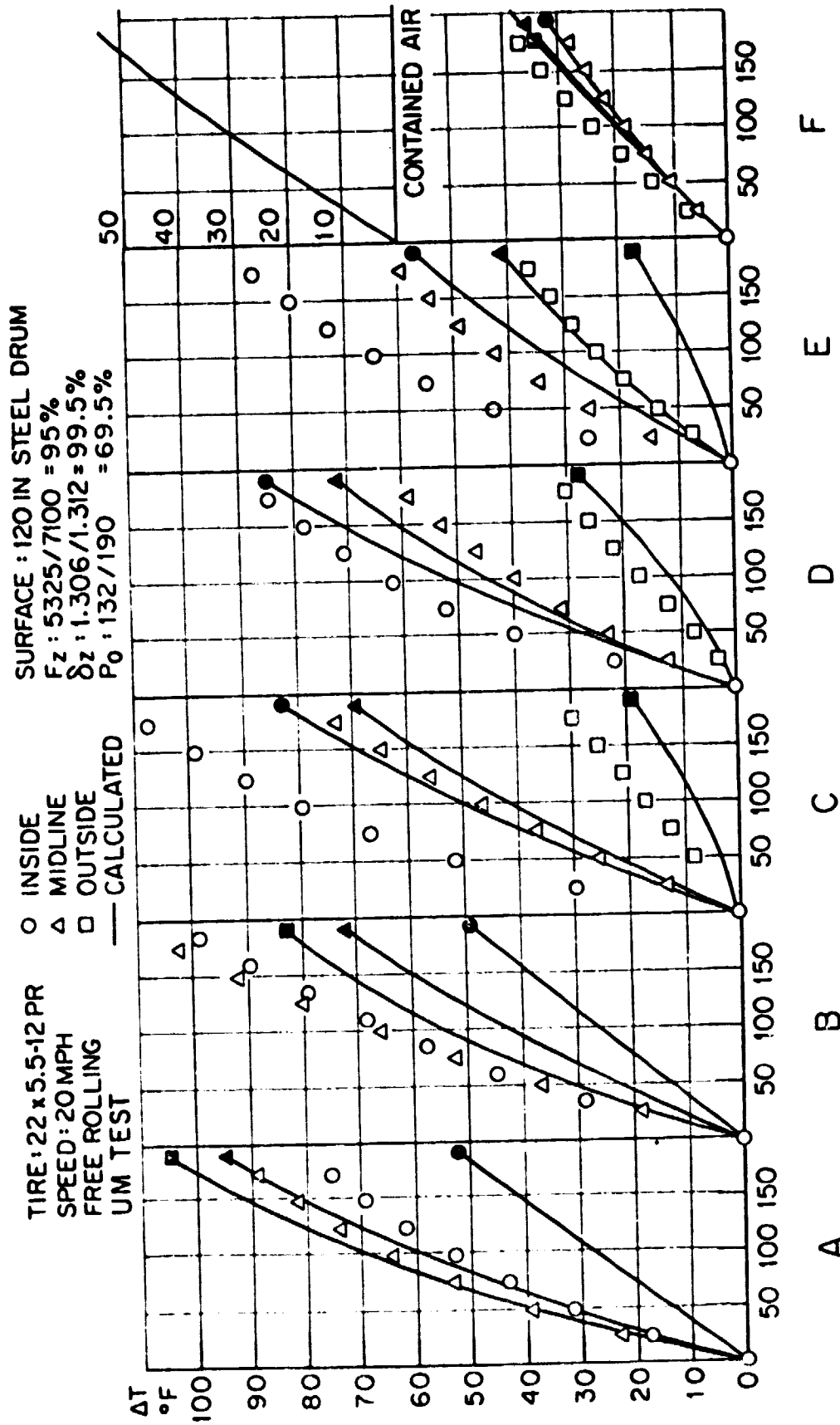


Fig. 25: Measured and Calibrated Tire Temperature Profiles.

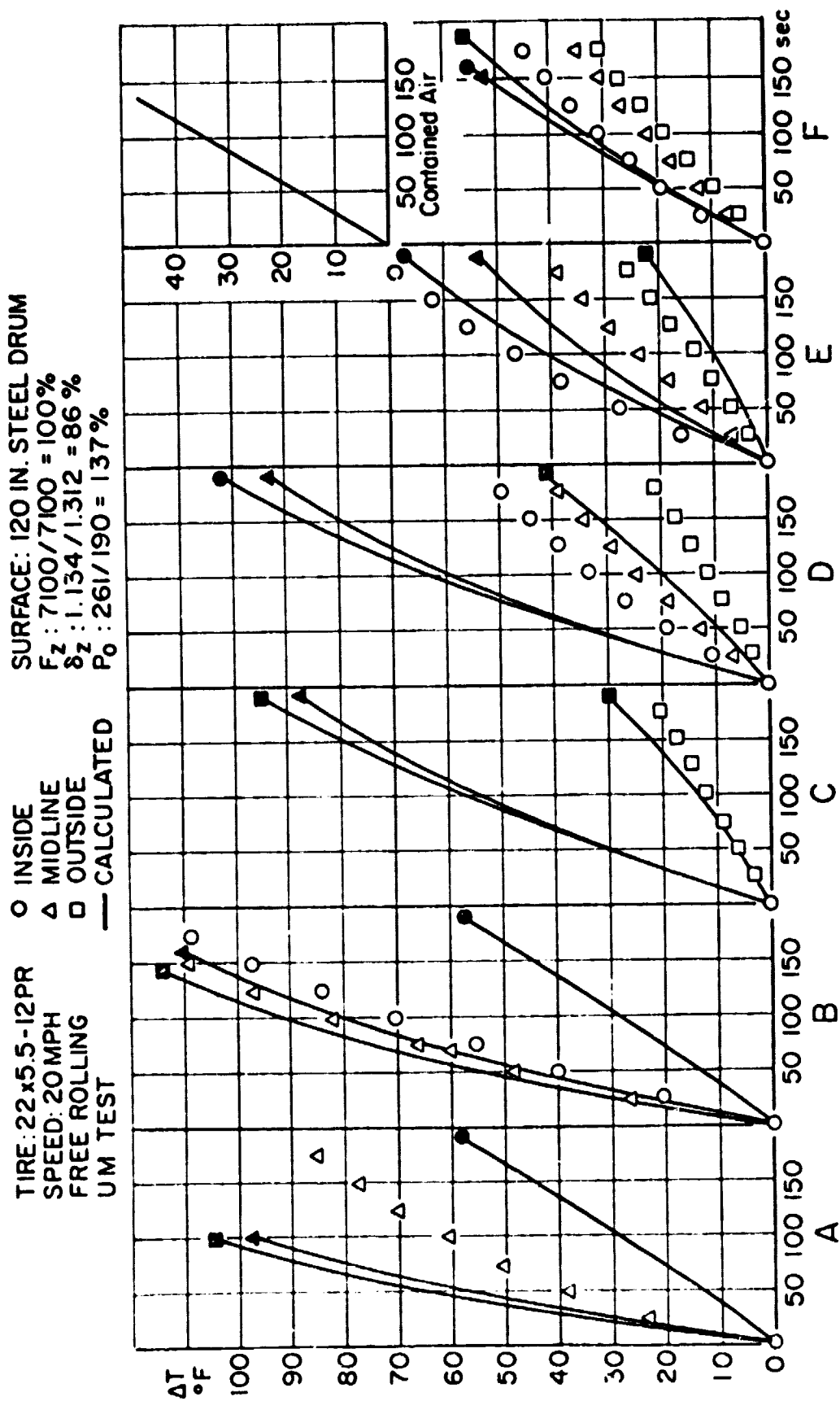


Fig. 26: Measured and Calibrated Tire Temperature Profiles.

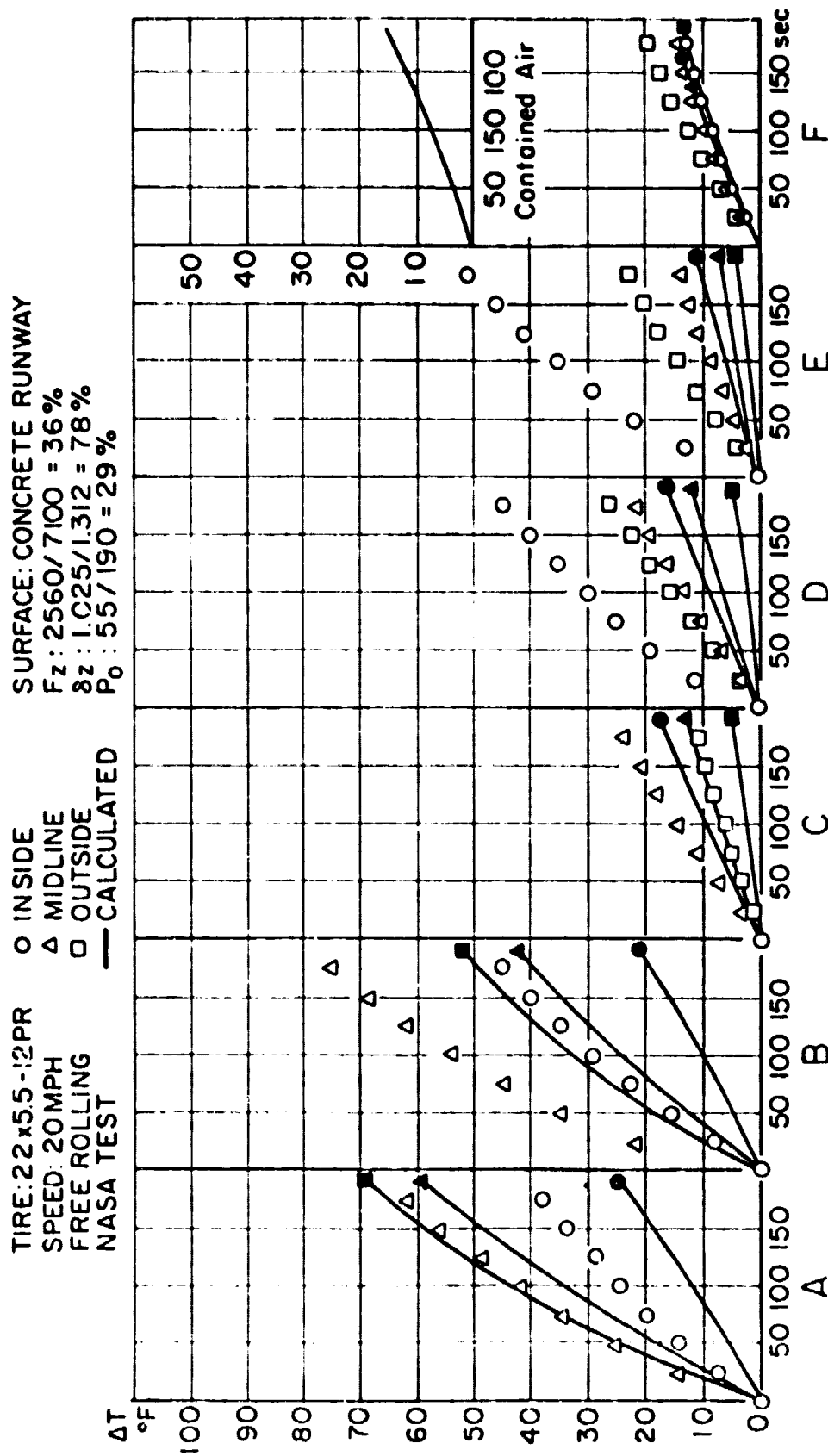


Fig. 27: Measured and Calibrated Tire Temperature Profiles.

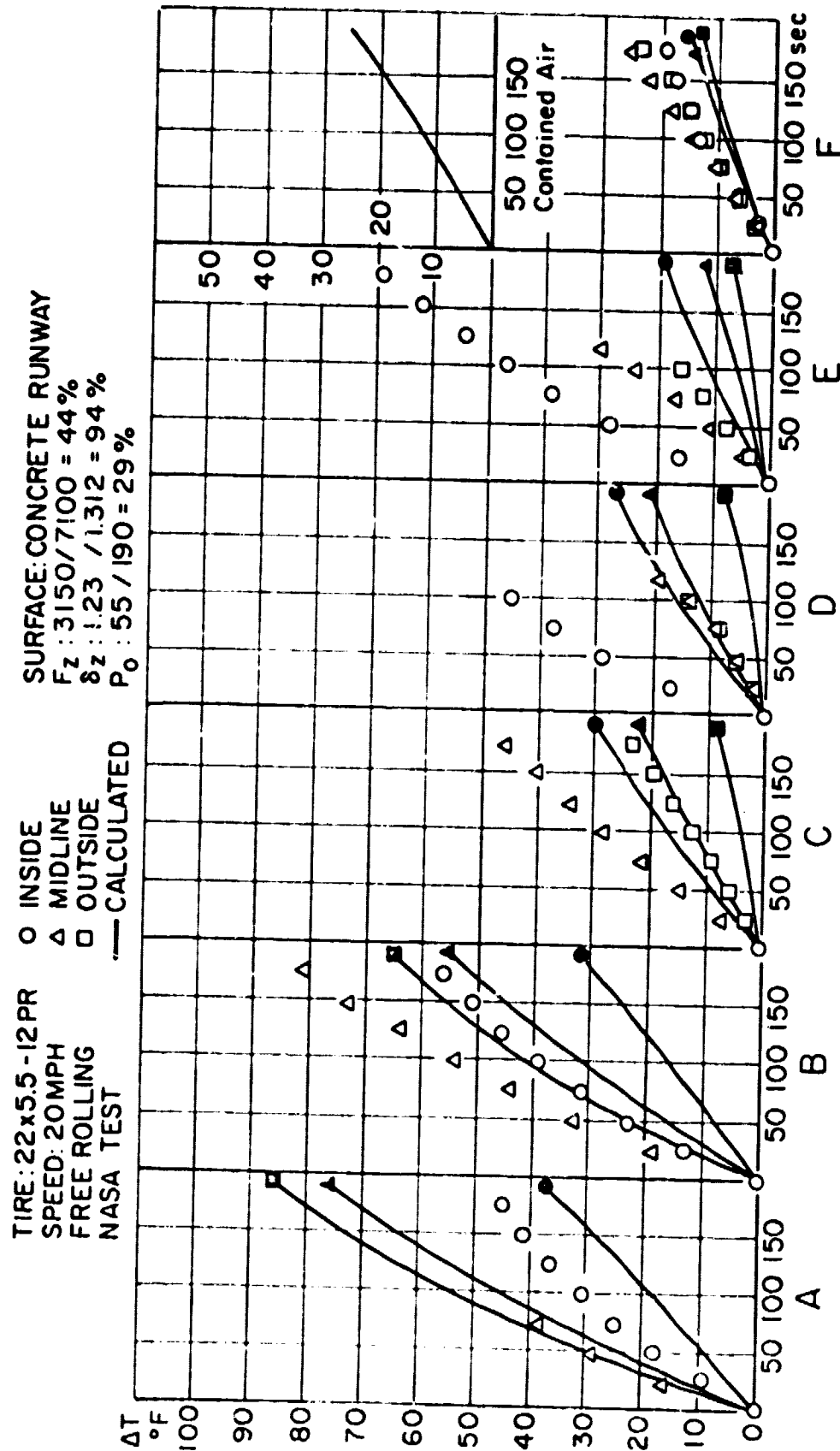


Fig. 28: Measured and Calibrated Tire Temperature Profiles.

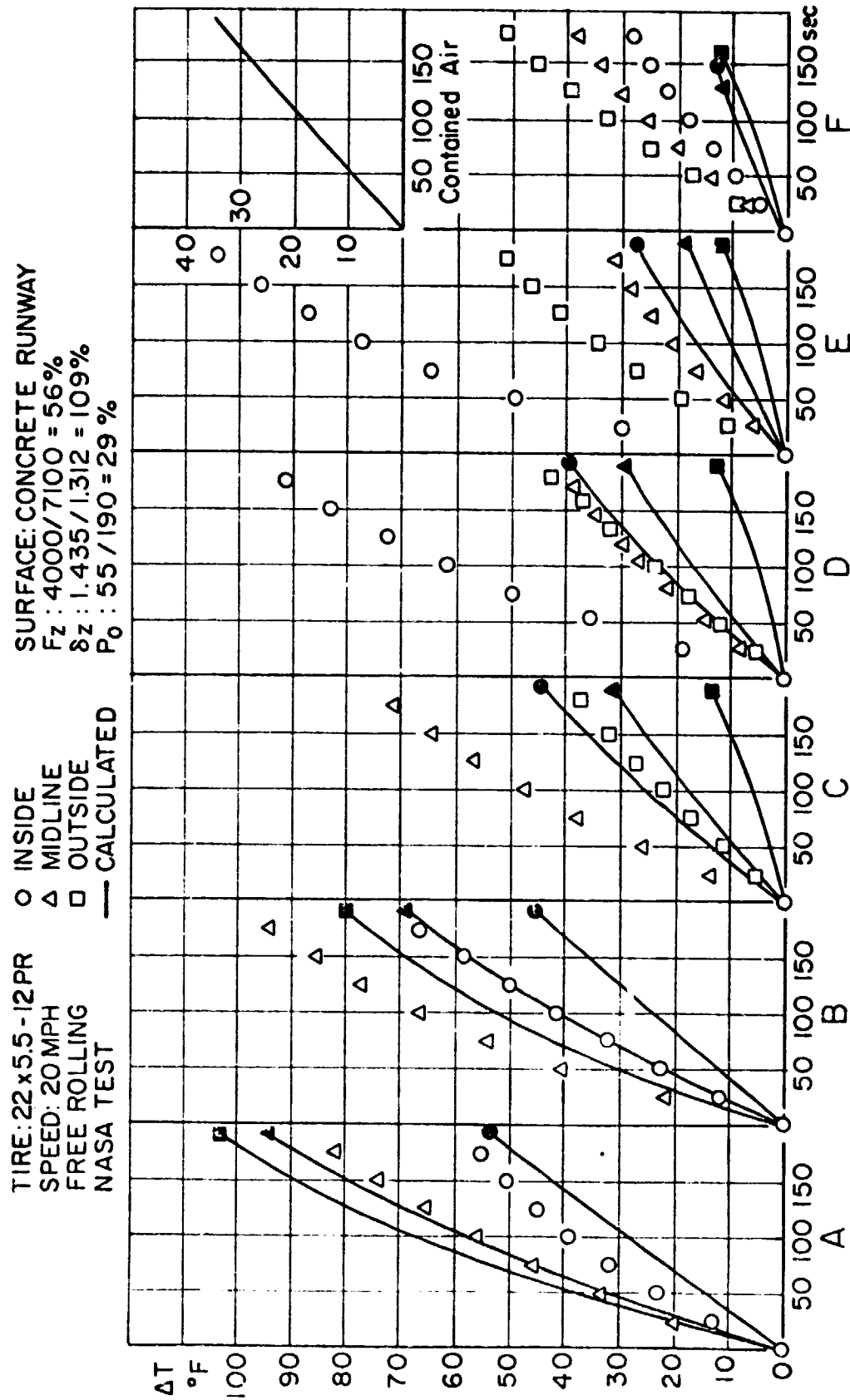


Fig. 29: Measured and Calibrated Tire Temperature Profiles.

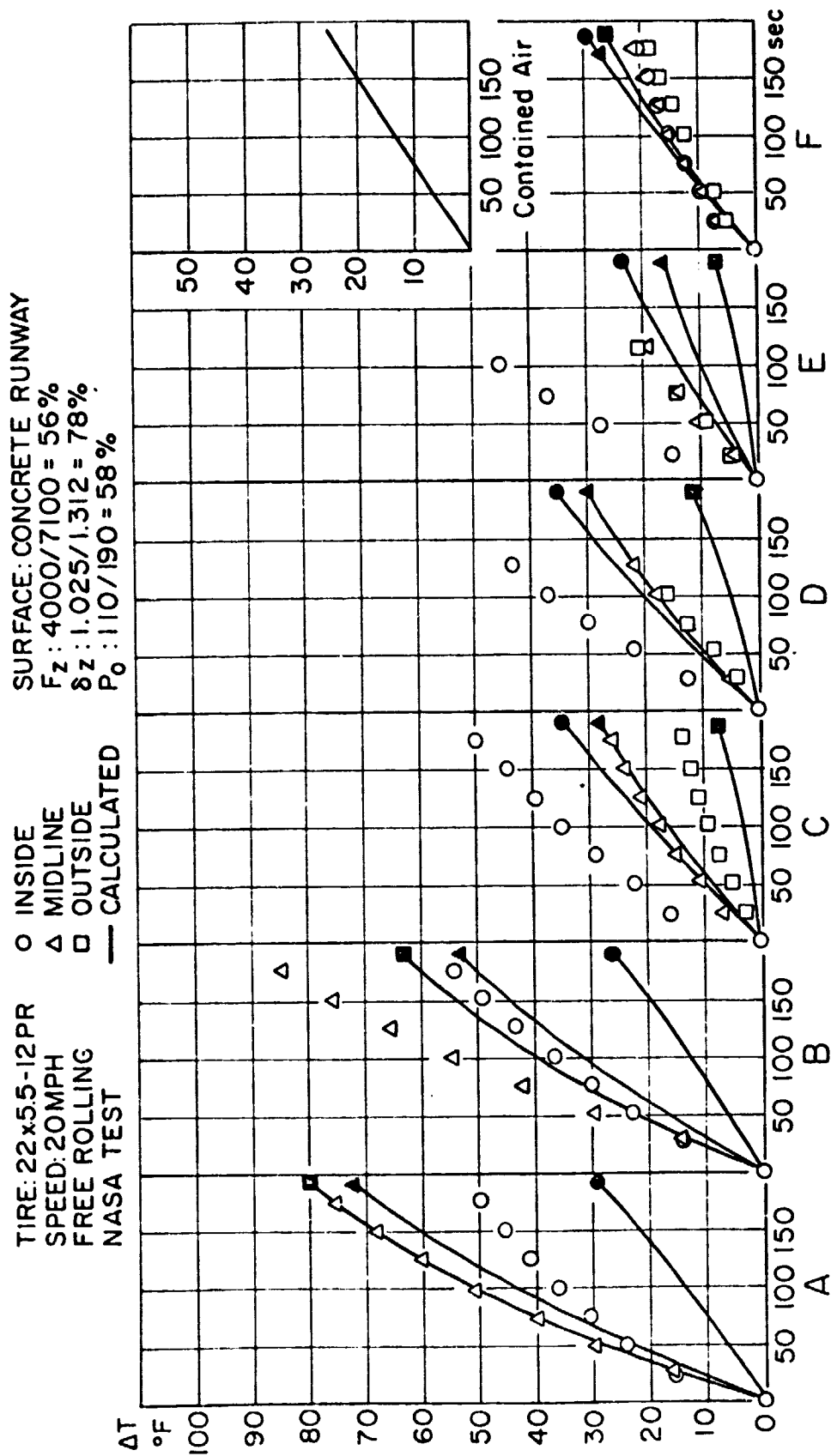


Fig. 30: Measured and Calibrated Tire Temperature Profiles.

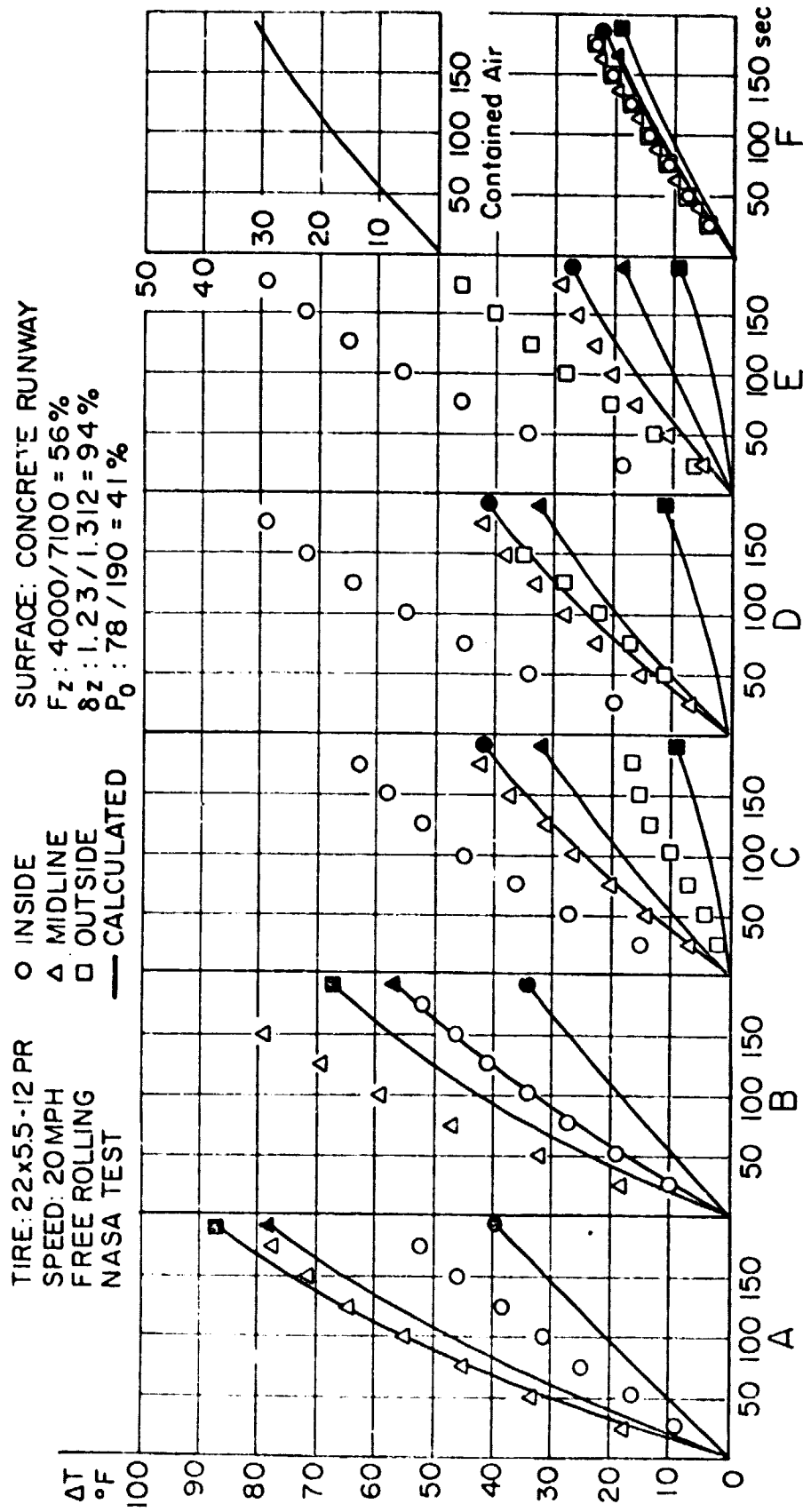


Fig. 31: Measured and Calibrated Tire Temperature Profiles.

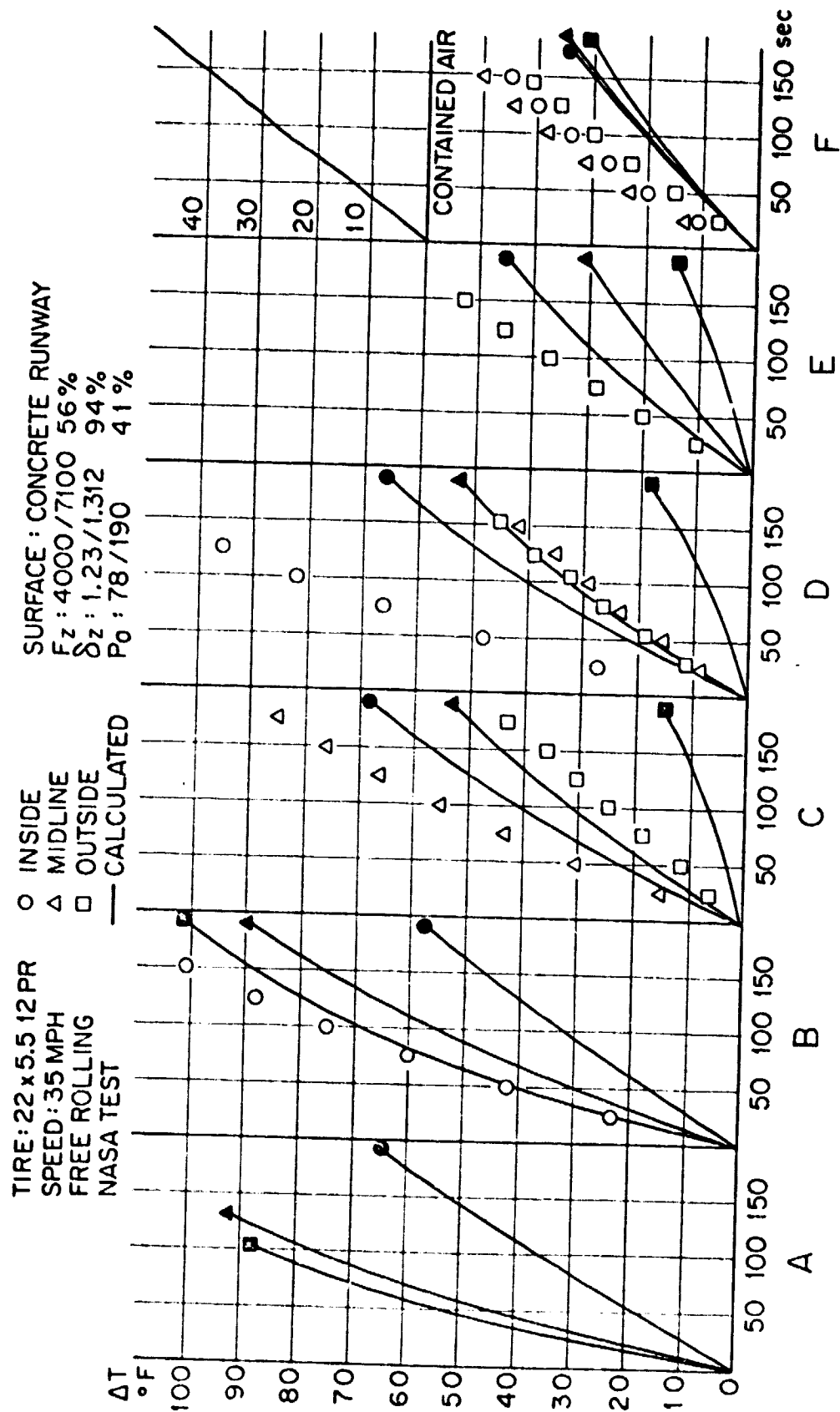


Fig. 33: Measured and Calibrated Tire Temperature Profiles.

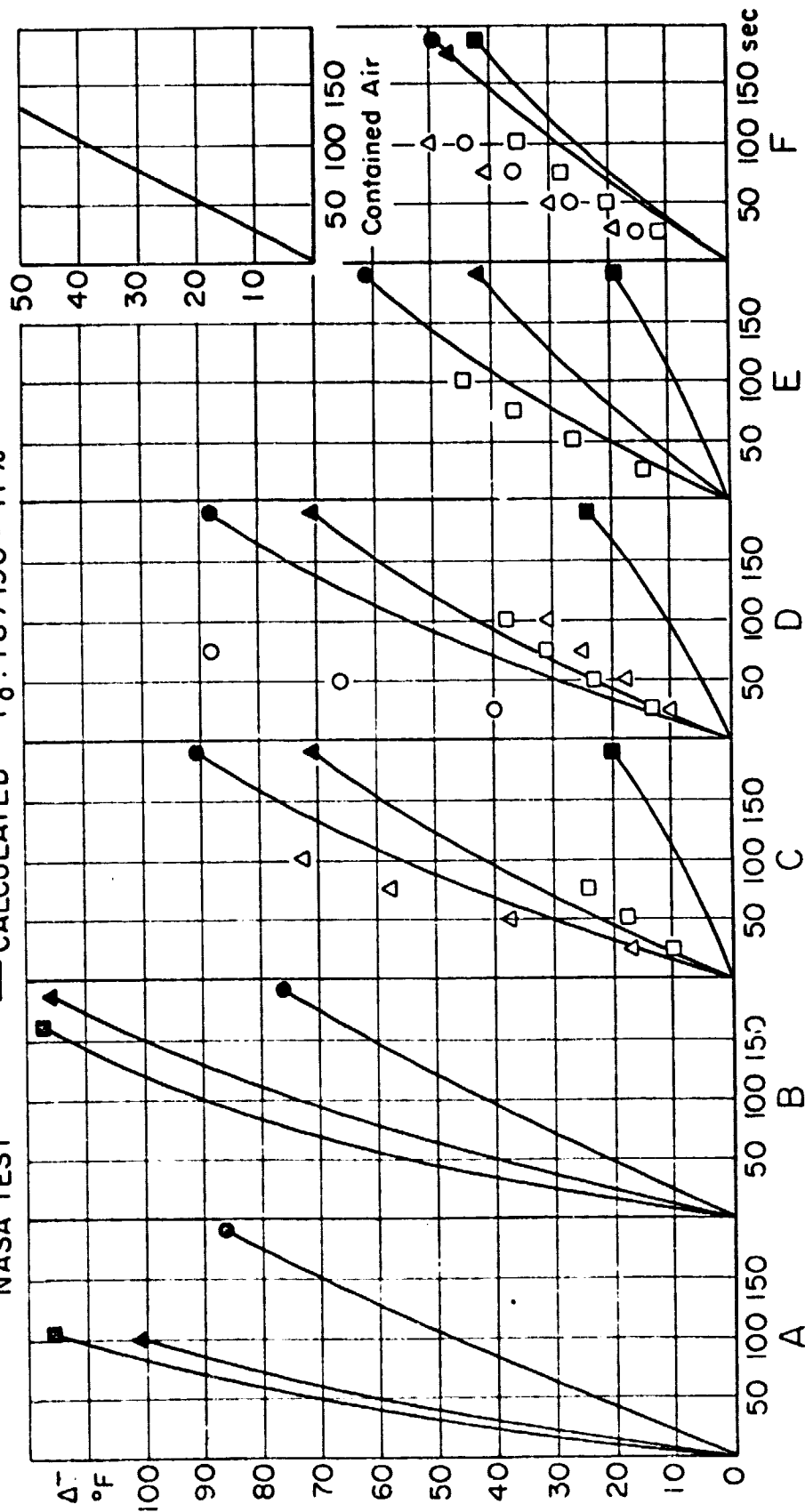


Fig. 33: Measured and Calibrated Tire Temperature Profiles.

REFERENCES

1. Conduction of Heat in Solids, Carslaw, H.S. and J.C. Jaeger, Oxford University Press, 1959.
2. Clark, S.K. "Plane Elastic Characteristics of Cord Rubber Composites". Textile Res. Jour.
3. Dodge, R. N. and S. Shaw, unpublished data
4. Walter, J.W. "Cord Rubber Tire Composites" Rubber Chem. and Tech., V. 51, N. 3, July-August 1978, p. 524.

APPENDIX A

Idealized Cross-Section Curvatures

It is assumed that the geometry of the tire carcass can be described by two intersecting circular arcs. For the undeformed tire these arcs describe the carcass centerline from the crown of the tire to the shoulder, R_c , and from the shoulder to the bead, R_1 , as shown in Figure A1.

It is assumed that the x-y coordinates of the shoulder (x_c, y_c) and bead (x_B, y_B) , the y-coordinate of the carcass at the crown, y_m , and the length of the carcass centerline from the shoulder to the bead, S_L , are known. All of these geometric properties can be measured from appropriate tire cross-section profiles. The location of the shoulder is somewhat arbitrary. However, for this analysis x_c was taken to be 0.75 of the section half-width w , and y_c to be the intersection of $x=x_c$ and the carcass centerline.

From geometry:

$$R_c = \frac{x_c^2 + (y_c - y_m)^2}{2(y_m - y_c)} \quad (A1)$$

$$\theta_c = \sin^{-1}\left(\frac{x_c}{R_c}\right) \quad (A2)$$

$$S_c = R_c \cdot \theta_c \quad (A3)$$

To find the radius of curvature of the undeflected sidewall one must first determine H:

$$H = \sqrt{(x_c - x_B)^2 + (y_c - y_B)^2} \quad (A4)$$

Noting that $R_1 = S_L/\theta$ and that $H/2 = R_1 \sin(\frac{\theta}{2})$, the angle θ can be found from:

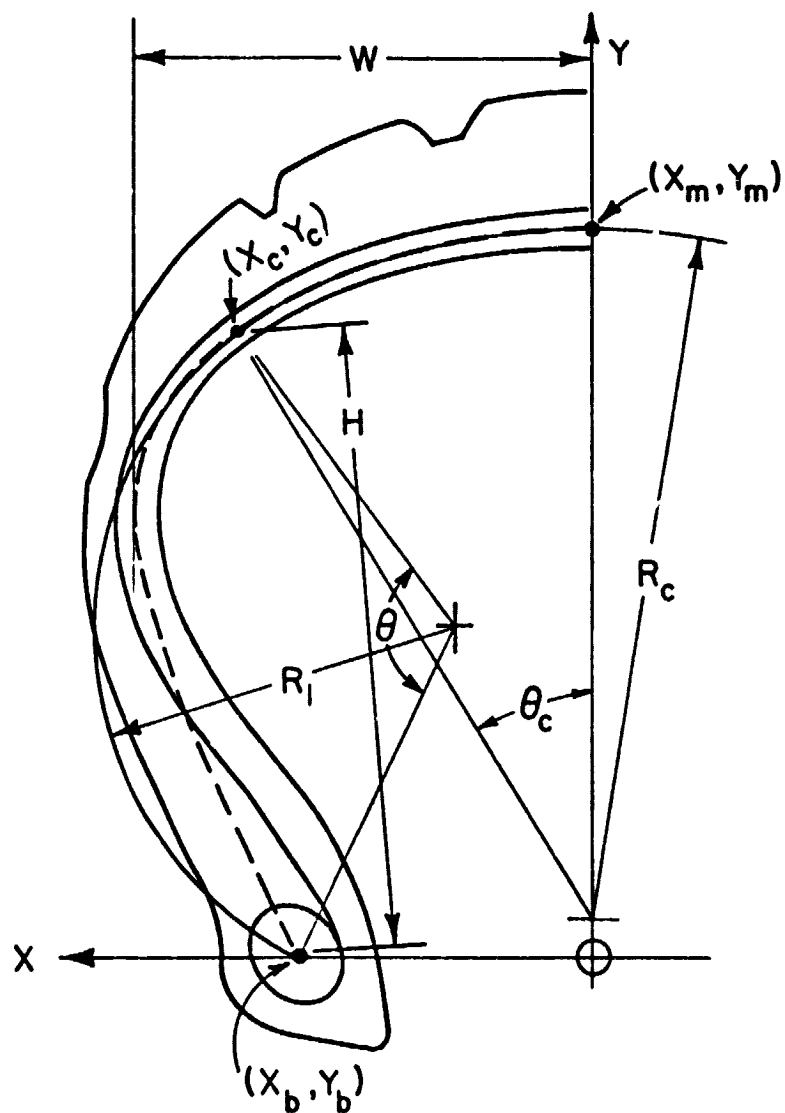


Figure A1 - Tire Cross-Section Illustrating Idealized Curvatures R_c and R_l

$$\theta - \frac{2S_L}{H} \sin\left(\frac{\theta}{2}\right) = 0 \quad (A5)$$

Solving (A5) for θ then allows the calculation of R_1 .

To calculate the radius of the deflected sidewall it is first assumed that the deflection is greater than $y_m - y_c$ and that the carcass changes from a circular arc of R_c to a flat surface of half-length S_c . It is thus assumed that the x-coordinate of the shoulder in the deflected position is S_c and the y-coordinate is $(y_m - \Delta)$. With the new co-ordinates of x_c and y_c a new H can be calculated from A4. However, before a final radius of curvature of the sidewall can be determined, one must account for the approximate change in the arc length S_L . This change takes place because there is a significant strain in the meridional direction for the operating conditions usually encountered in aircraft tire service.

Referring to Figure A2, the final length of the carcass centerline is:

$$S_f = S_L(1 + \epsilon_\phi)$$

where ϵ_ϕ is the meridional strain. This strain is approximately:

$$\epsilon_\phi = \frac{P_o}{h_c E_\phi} (R_f - R_1)$$

Thus:

$$S_f = S_L \left(1 + \frac{P_o}{h_c E_\phi} (R_f - R_1) \right) \quad (A6)$$

where P_o is the internal pressure and $E_\phi h_c$ is the average stiffness of the sidewall in the meridional direction. Also from the figure:

$$R_f \sin\left(\frac{\theta_f}{2}\right) = \frac{H_f}{2} \quad (A7)$$

and

$$\theta_f = \frac{S_f}{R_f} \quad (A8)$$

Substituting from (A6) and (A8) into (A7):

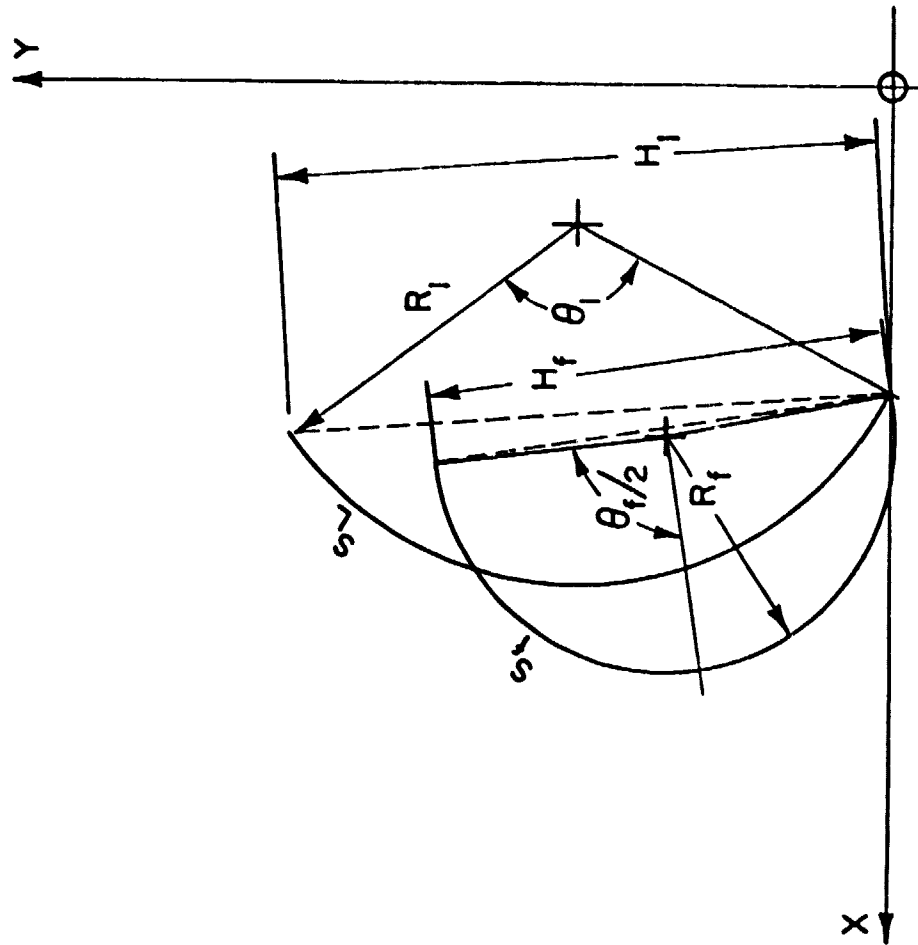


Figure A2 - Geometry of original and final idealized curvatures

$$R_f \sin \left[\frac{S_L \left(1 + \frac{P_o}{E h c} (R_f - R_1) \right)}{2R_f} \right] - \frac{H_f}{2} = 0 \quad (A9)$$

The solution of this transcendental equation for R_f gives the radius of curvature of the deflected sidewall.

APPENDIX B

Bead Tension Analysis

Consider the sidewall of an aircraft tire as shown in Fig. B1, first in the undeformed and then in the deformed state.

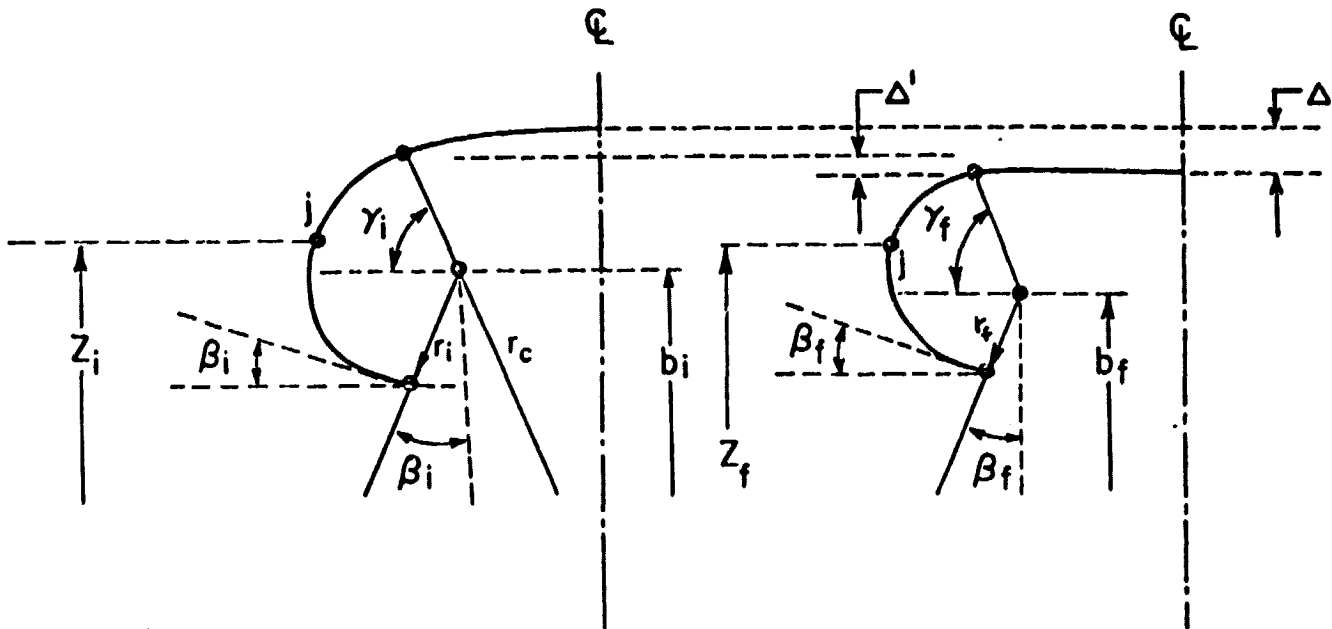


Figure B1. Sidewall geometry used in bead tension analysis.

The membrane forces in the ϕ direction are given in Eq. (15).

$$N_{\phi_i} = \frac{P_o}{2} \left[r_i \left(1 + \frac{b_i}{z_i} \right) \right]$$

$$N_{\phi_f} = \frac{P_o}{2} \left[r_f \left(1 + \frac{b_f}{z_f} \right) \right]$$

The angle β_1 is given from initial tire geometry. From Fig. B1

$$2r_i \cos \beta_i - 2r_f \cos \beta_f = \Delta' \quad (B1)$$

or

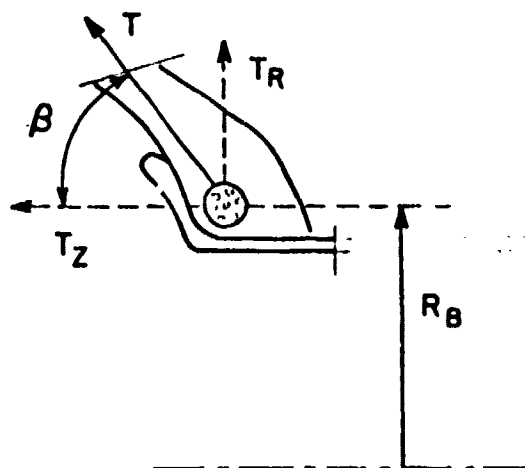
$$\cos \beta_f = \frac{2r_i \cos \beta_i - \Delta'}{2r_f} \quad (B2)$$

Also

$$\Delta' = \Delta - r_c(1 - \cos \lambda) \quad (B3)$$

Using geometry previously developed in Appendix A, Δ' can be found from Eq. (B3), and β_f from Eq. (B2).

Bead tension may be split into radial and axial components as in Fig. B2. The axial component T_z is carried by the wheel flange. The radial component causes bead tension in the amount



$$T_R = (N_\phi \sin \beta) R_B \quad (B4)$$

using a uniformly loaded ring

The difference in bead tensions between points A and B of Fig. 2 is given by

Fig. B2

$$T_{R_f} - T_{R_i} = (N_{\phi_f} \sin \beta_f - N_{\phi_i} \sin \beta_i) R_B \quad (B5)$$

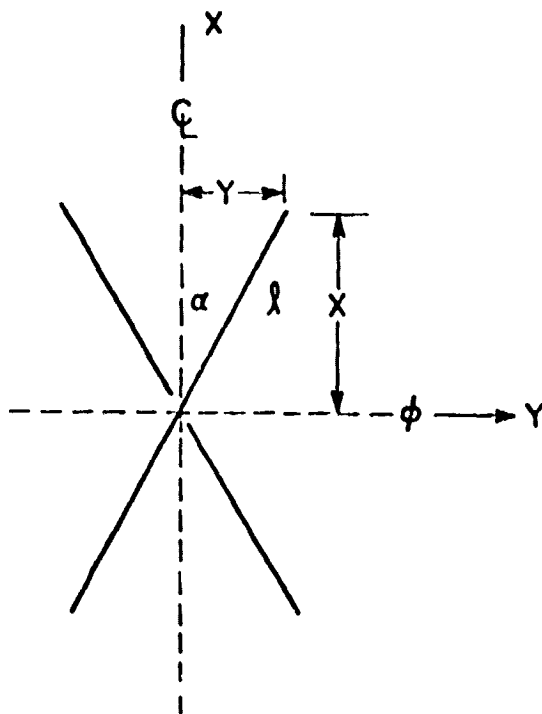
Denote the gross area of the bead wires as A_B , and the modulus of the bead bundle based on this gross area as E_B . Then the strain energy stored during one half cycle is

$$U_V = \frac{1}{2} (T_{R_f} - T_{R_i})^2 / (A_B^2 E_B) \quad (B6)$$

APPENDIX C

Aircraft tire construction is entirely bias ply and the ply angles span a limited range, say between 30° and 60° for half angles α as illustrated in Fig. 8. Previous studies by the authors [2,3] and by Walter [4] have shown that within this range of angles the elastic constants of the composite bias ply structure are well represented by a simplified analytical model using cords which are inextensible but which are encased in an elastic matrix.

Consider the bias cord structure of Fig. C1.



Assuming inextensible cord,

$$x = l \cos \alpha$$

$$dx = -l \sin \alpha d\alpha$$

$$\epsilon_x = \frac{dx}{x} = -\tan \alpha d\alpha$$

$$y = l \sin \alpha;$$

$$dy = l \cos \alpha d\alpha$$

$$\epsilon_y = \frac{dy}{y} = \cot \alpha d\alpha$$

Fig. C1

Detail of idealized bias net structure.

$$\epsilon_x = \epsilon_y \tan^2 \alpha \epsilon_\phi, \text{ or}$$

$$\epsilon_\theta = \tan^2 \alpha \epsilon_\phi$$

$$\frac{\epsilon_\theta}{\epsilon_\phi} = \tan^2 \alpha = \mu_{\theta\phi} \quad (C1)$$

$$\cot^2 \alpha = \mu_{\phi\theta} \quad (C2)$$

Calculate the modulus of elasticity, assuming energy storage by rubber only.

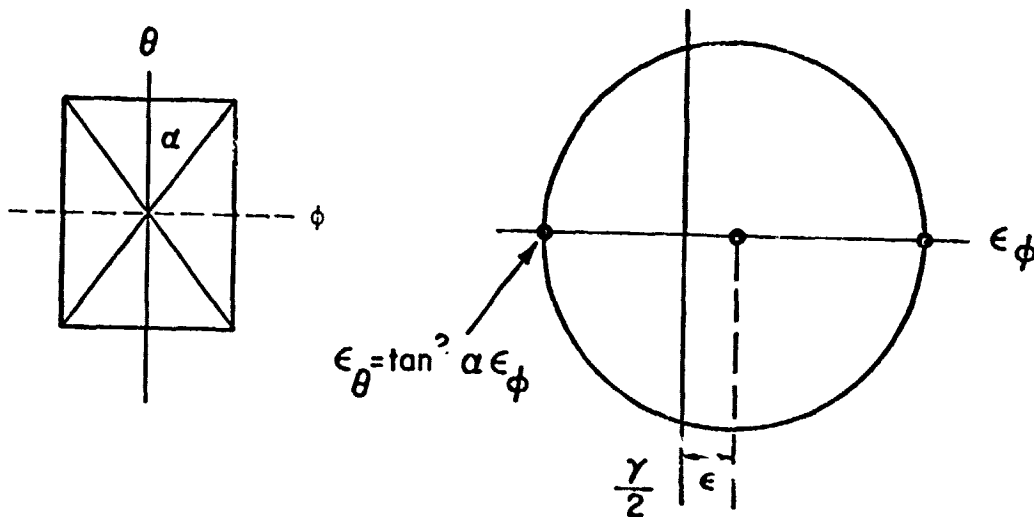


Fig. C2.

Mohr's circle for idealized net structure.

The radius of Mohr's circle is $\epsilon_\phi \frac{(1+\tan^2\alpha)}{2} = (\gamma/2)$. The center is located at $\frac{(1-\tan^2\alpha)}{2}\epsilon_\phi = \epsilon$

The element is now subjected to both shear γ and extension ϵ .

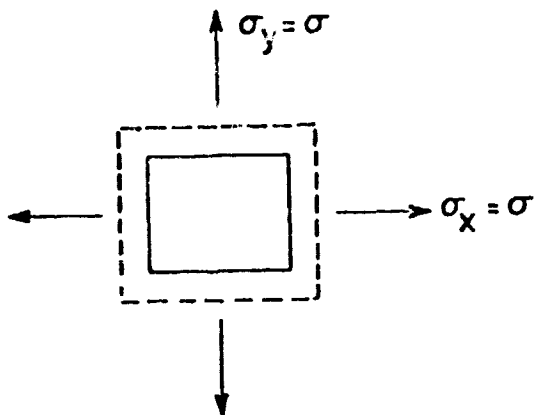
Express the strain energy as

$$V = \frac{1}{2} \epsilon_x \sigma_x + \frac{1}{2} \epsilon_y \sigma_y + \frac{1}{2} \gamma_{xy} \tau_{xy}$$

But $\tau_{xy} = G\gamma_{xy}$ and also due to isotropy

$$\epsilon = \frac{\sigma}{E} - \mu \frac{\sigma}{E} = \frac{0.5\sigma}{E}$$

$$\sigma = 2E\epsilon$$



$$\text{But } G = \frac{E}{2(1+\mu)} = \frac{E}{3}$$

$$E = 3G$$

$$\sigma = 6G\epsilon$$

The strain energy is now

$$\begin{aligned}
 V &= \frac{1}{2} \cdot 6G\epsilon^2 + \frac{1}{2} 6G\epsilon^2 + \frac{1}{2} G\gamma^2 \\
 &= \frac{1}{2} [12G \cdot (\frac{1-\tan^2\alpha}{4})^2 + G(1+\tan^2\alpha)^2] \epsilon_\phi^2
 \end{aligned}$$

$$\frac{\partial V}{\partial \epsilon_\phi} = E_\phi \cdot \epsilon_\phi = 4G[1-\tan^2\alpha + \tan^4\alpha] \epsilon_\phi^2$$

$$E_\phi = 4G[1-\tan^2\alpha + \tan^4\alpha] \quad (C3)$$

$$\text{Also } \tan(90-\alpha) = \cot \alpha; E_\theta = 4G[1-\cot^2\alpha + \cot^4\alpha] \quad (C4)$$

This agrees well with more exact expressions of Refs. [2-4].

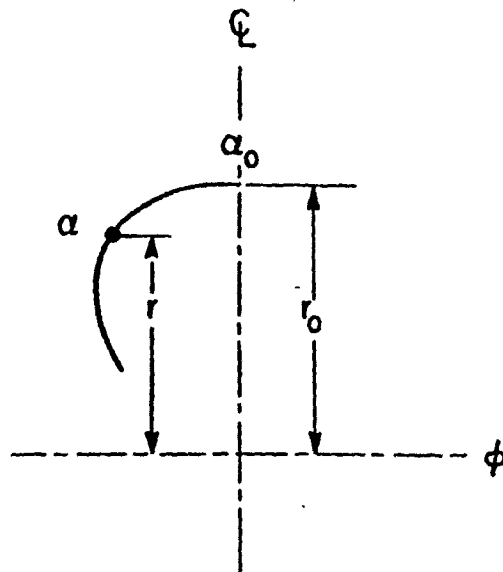
The angle distribution in a bias ply aircraft tire is given by

$$\cos \alpha = \frac{r}{r_o} \cos \alpha_o$$

where

α_o = crown angle

r_o = crown radius

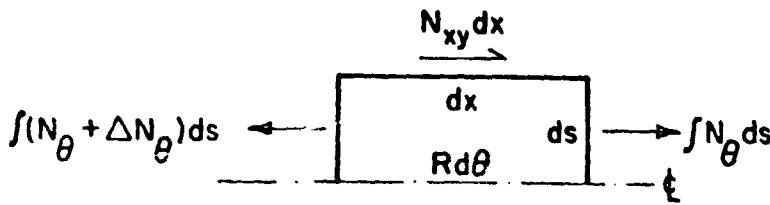


APPENDIX D

Sidewall Membrane Shear

The membrane forces N_ϕ and N_θ vary as the tire rolls through the contact patch. The variation in N_θ causes a shear stress to be required for equilibrium purposes. This shear stress gives rise to an energy storage, hysteretic loss and heat generation process which is similar to those found by other mechanisms.

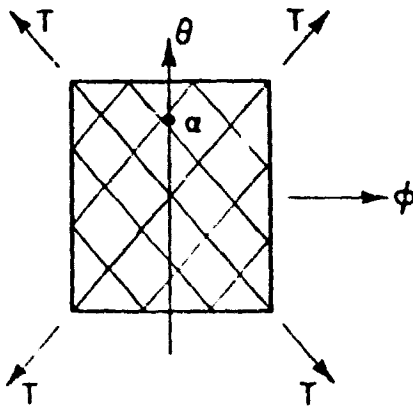
Consider the tire cut at its centerline and spread out flat as shown in Fig. D1. Equilibrium of forces requires the



existence of a membrane shear force N_{xy} as shown. This is caused by the variation in N_θ with circumferential position.

Fig. D1, Idealized view of tire section.

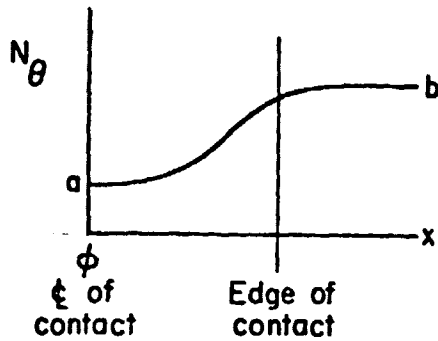
Next consider the relation between N_θ and N_ϕ . For a net structure in which loads are carried by the cords alone, Fig. D2 illustrates the division of cord load between N_ϕ and N_θ . If T represents a typical cord load, it may be shown that



$$\frac{N_\phi}{N_\theta} = \tan^2 \alpha \quad N_\theta = N_\phi \cot^2 \alpha \quad (D1)$$

Fig. D2. Idealized net structure.

Since N_ϕ is calculated as part of the contribution to strain energy in the sidewall regions I and III, then it is available for computation of N_θ . At any location the variation of N_θ follows the variation of N_ϕ , which is approximately of the form shown in Fig. D3.



Letting the variation of N_θ with respect to circumferential position x be approximated by

$$N_\theta = a + b(1 - e^{-c^2 x^2}) \quad (D2)$$

Fig. D3. Variation of N_θ with circumferential position.

$$\text{where } a = (N_\phi)_B^* \cot^2 \alpha \quad b = [(N_\phi)_A^* - (N_\phi)_B] \cot^2 \alpha$$

$$c^2 \approx \frac{1}{w^2} \quad \text{where } w = \text{section width.}$$

Since the maximum value of N_{xy} depends on the maximum gradient of N_θ , then it can be determined by differentiation of Eq. D2.

$$\frac{dN_\theta}{dx} = 2bc^2 x e^{-c^2 x^2}$$

$$\frac{d^2 N_\theta}{dx^2} = 2bc^2 [1 - 2c^2 x^2] e^{-c^2 x^2}$$

$$\text{The maximum of } \frac{dN_\theta}{dx} \text{ occurs at } x = \frac{1}{c\sqrt{2}}$$

*See Fig. 2 for location of points A and B.

and results in

$$\begin{aligned} \left(\frac{dN_{\theta}}{dx}\right)_{\max} &= 2b \frac{c^2}{c\sqrt{2}} e^{-\frac{1}{2}} = 0.858 \frac{b}{w} \\ &= \frac{0.858}{w} [(N_{\theta})_A - (N_{\theta})_B] \cot^2 \alpha \end{aligned} \quad (D3)$$

From plane equilibrium,

$$\frac{dN_{\theta}}{dx} = \frac{dN_{xy}}{dy} \quad (D4)$$

so that

$$dN_{xy} = \frac{0.858}{w} [(N_{\phi})_A - (N_{\phi})_B] \cot^2 \alpha \cdot dy, \text{ where } y$$

is measured along the circumference of the tire meridian. $\cot \alpha$ varies with this position, so that the net value of N_{xy} at any computational cell is given by

$$N_{xy} = \frac{0.858}{w} [(N_{\phi})_A - (N_{\phi})_B] \int^i \cot^2 \alpha \cdot dy \quad (D5)$$

From this the strain energy can be formed

$$U = \frac{1}{2} N_{xy}^2 / h^2 G_{xy} \quad (D6)$$

APPENDIX E

Contact Pressure Analysis

Independent of other effects, the tire cycles between zero tread compressive stress and a maximum compressive stress.

Measurements indicate a maximum pressure/unit length at the b of contact, approximating 1.25 x average inflation pressure x width.

Examine three possible pressure distributions, all giving rise to the same load/unit length. See Fig. E-1.

$$\text{Stored energy} \sim \frac{p^2}{E} \sim \int_{-w/2}^{w/2} p^2 dy \quad \text{assuming } E = \text{constant across the tread.}$$

$$(a) \quad E_a = \int_0^w (1.25p_o)^2 dy = 1.5625p_o^2 w \quad \text{for constant pressure} \quad (E1)$$

$$(b) \quad \text{Parabola 1: } p = p_m \left[1 - \left(\frac{2y}{w} \right)^2 \right]$$

$$E_b = \int_{-w/2}^{w/2} p^2 dy = p_m^2 \left\{ y - \frac{8y^3}{3w^2} + \frac{16y^5}{5w^4} \right\} \bigg|_{-w/2}^{w/2} = p_m^2 \cdot \frac{8}{15} w \quad (E2)$$

$$\text{But } \int_{-w/2}^{w/2} p dy = 1.25 p_o w = \int_{-w/2}^{w/2} p_m \left[1 - \frac{4y^2}{w^2} \right] dy = \frac{2p_m w}{3}$$

$$\therefore p_m = \frac{3}{2} \times 1.25 p_o \quad (E3)$$

$$\therefore E_b = p_m^2 \times \frac{8}{15} w = \frac{9}{4} \times \frac{25}{16} p_o^2 \times \frac{8}{15} w = 1.875 p_o^2 w = 1.2 \times E_a \quad (E4)$$

(c) Parabola 2: $p = p_m \left(\frac{4y^2}{w^2} \right)$

$$\int_{-w/2}^{w/2} p dy = 1.25 p_o w = p_m \int \frac{4y^2}{w^2} dy = p_m \left. \frac{4y^3}{3w^2} \right|_{-w/2}^{w/2}$$

$$E_c = \int p^2 dy = p_m^2 \int \frac{16y^4}{w^4} dy = p_m^2 \frac{w}{5} = 2.8125 p_o^2 w = 1.80 E_a$$

We adopt a conservative value of $\frac{1.80+1.20}{2} = 1.5 \times \text{uniform}$ case. Assume uniform contact pressure of $1.25 \times p_o$. Then multiply by 1.5 factor for shape distribution.

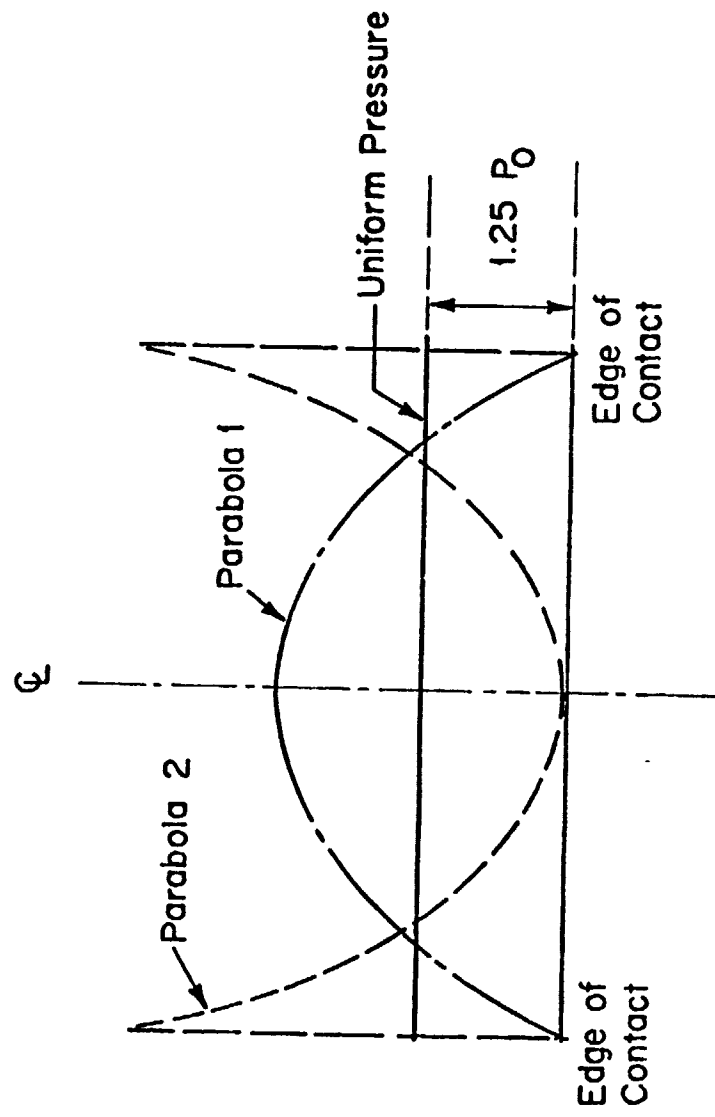
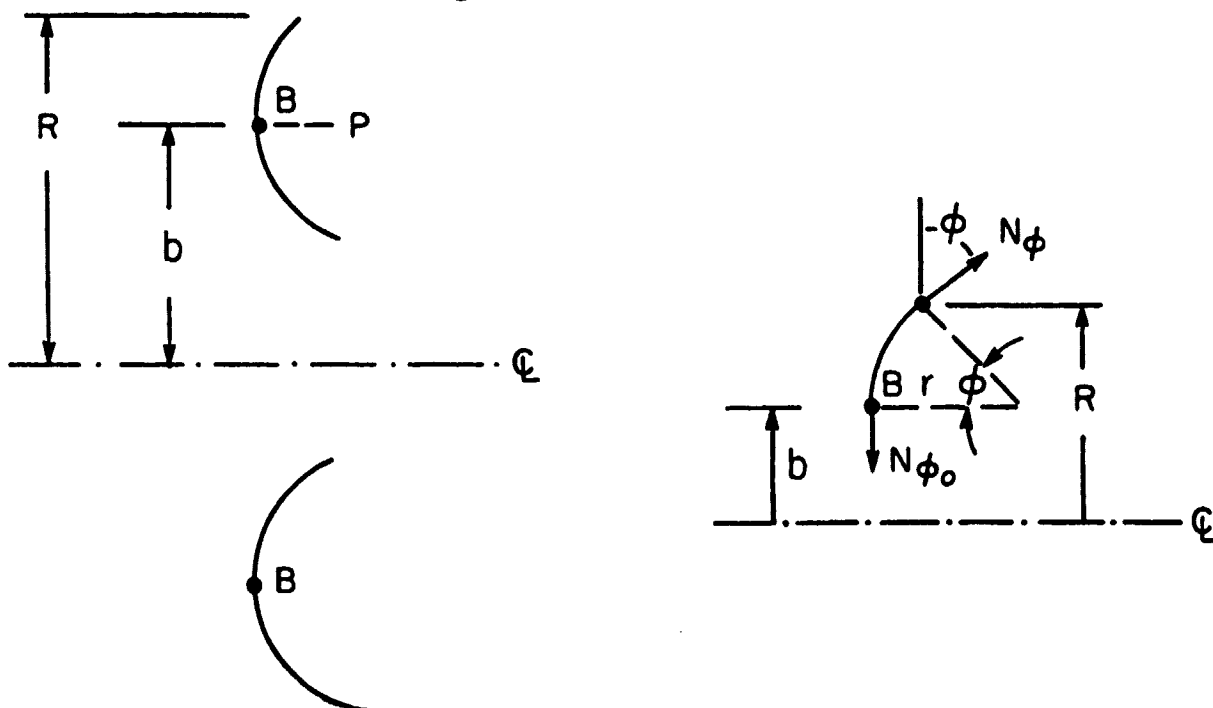


Fig. E-1. Transverse Pressure Distributions

APPENDIX F

Meridional Membrane Strains

Consider the meridional membrane stresses in a torus of circular cross section as shown in Fig. F1, subject to an internal pressure p . Cut out a section bounded by a vertical tangent point, distance b from the axis L , and a general point R . This is shown in Fig. F2.



Horizontal equilibrium of Fig. F2, considering the entire axisymmetric ring, leads to the expression.

$$N_{\phi} \cdot 2\pi R \sin \phi = p \cdot \pi(R^2 - b^2) \quad (F1)$$

from which

$$\begin{aligned} N_{\phi_A} &= \frac{p(R+b)(R-b)}{2R \sin \phi} = \frac{p(R+b)(r \sin \phi)}{2R \sin \phi} \\ &= \frac{pr}{2} \left(1 + \frac{b}{R}\right) \quad (F2) \end{aligned}$$

During deformation of the tire into the center of the contact patch, point B of Fig. 2, the tire deflects but the sidewall remains a circular arc, although of reduced radius. The vertical tangent point B also shifts inward, so that both r and b in Eq. F2 take on new values. The final value of N still carries the same form, namely

$$N_{\phi_B} = \frac{pr_f}{2} \left(1 + \frac{b_f}{R_f} \right) \quad (F3)$$

where r_f , b_f and R_f define the same material point previously denoted by r , b and R . The change in N_{ϕ} now becomes

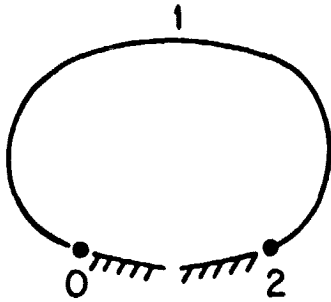
$$\Delta N_{\phi} = N_{\phi_A} - N_{\phi_B} \quad (F4)$$

This is the stress change upon which the strain energy is based.

APPENDIX G

Contained Air Temperature

Consider the tire cross-section as shown in Fig. G1. Let θ be the area weighted average of the temperatures on the inner surface of the tire over the region 0-1-2. Let y be the contained air temperature. Then the equation for temperature rise of the contained air is



$$c_p \cdot \rho \cdot V \frac{dy}{dt} = hA(\theta - y) \quad (G1)$$

Fig. G1.

where

- h = average heat transfer coefficient
- A = surface area of convection 0-1-2
- c_p = specific heat of air
- ρ = air density
- V = volume of contained air

Let $hA/c_p \rho V = \beta$. Then Eq. G1 becomes

$$\frac{dy}{dt} + \beta y = \beta \theta \quad (G2)$$

In the initial stages of tire heating the tire inner surface temperatures rise almost linearly, so that $\theta = ct$. In this case Eq. (G2) has a solution

$$y = \theta - \frac{c}{\beta}(1 - e^{-\beta t}) \quad (G3)$$

This solution lags behind the tire inner surface temperature.

For longer times when θ is determined numerically, the contained air temperature y must be calculated by the methods previously described using a finite difference form of Eq. (G1).

APPENDIX H

Geometry of 22 x 5.5 Tire

Figures H1 and H2 show the 22 x 5.5 8PR and the 22 x 5.5 12PR tires in cross-section used in the thermal analysis discussed below. For this analysis it is convenient to divide the half cross-section into eleven sections in which each section is in turn divided into three elements. As can be seen from the figure, each element is identified by two subscripts, the first one indicating the meridional location from bead to crown and the second indicating the location through the thickness from inside to outside. Many geometric values are required from this sectional profile in the analysis which follows. The definitions of such values are listed below and their numerical values for both tires are given in Tables H1 and H2.

V(I,J)	-	Volume of element
LH(I,J)	-	Area across which heat is transferred in thickness direction within the carcass
LV(I,J)	-	Area across which heat is transferred in the meridional direction within the carcass.
DH(I,J)	-	Distance between nodes through thickness
DV(I,J)	-	Distance between nodes meridional direction
AA(I)	-	Area across which heat is transferred to outside air
DA(I)	-	Distance from outside element nodes to outside surface
AC(I)	-	Area across which heat is transferred to contained air
DC(I)	-	Distance from inside element nodes to inside surface
R(I)	-	Radial location of each section from wheel centerline
YS(I,J)	-	Distance along meridian from crown to node of each element
Y(I,J)	-	Distance from inside surface of section to node of each element in the section
H1(I)	-	Thickness of carcass in each section
H2(I)	-	Thickness of rubber in each section

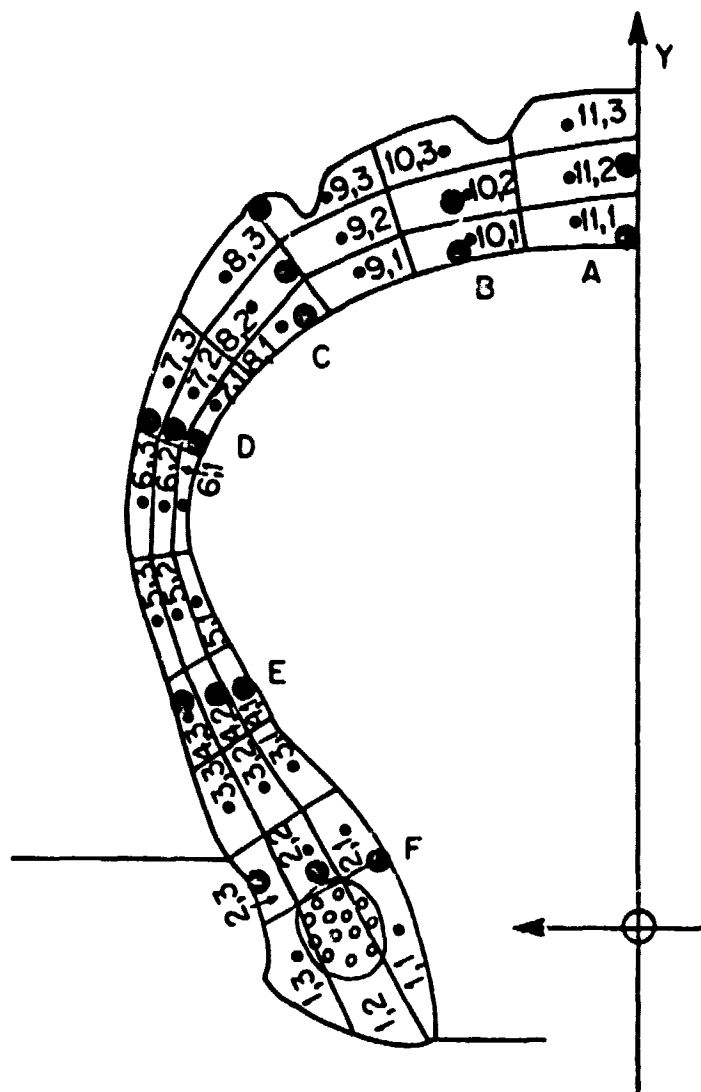


Figure H1. Element sectioning for Thermal Analysis. Solid dots represent approximate thermocouple locations.

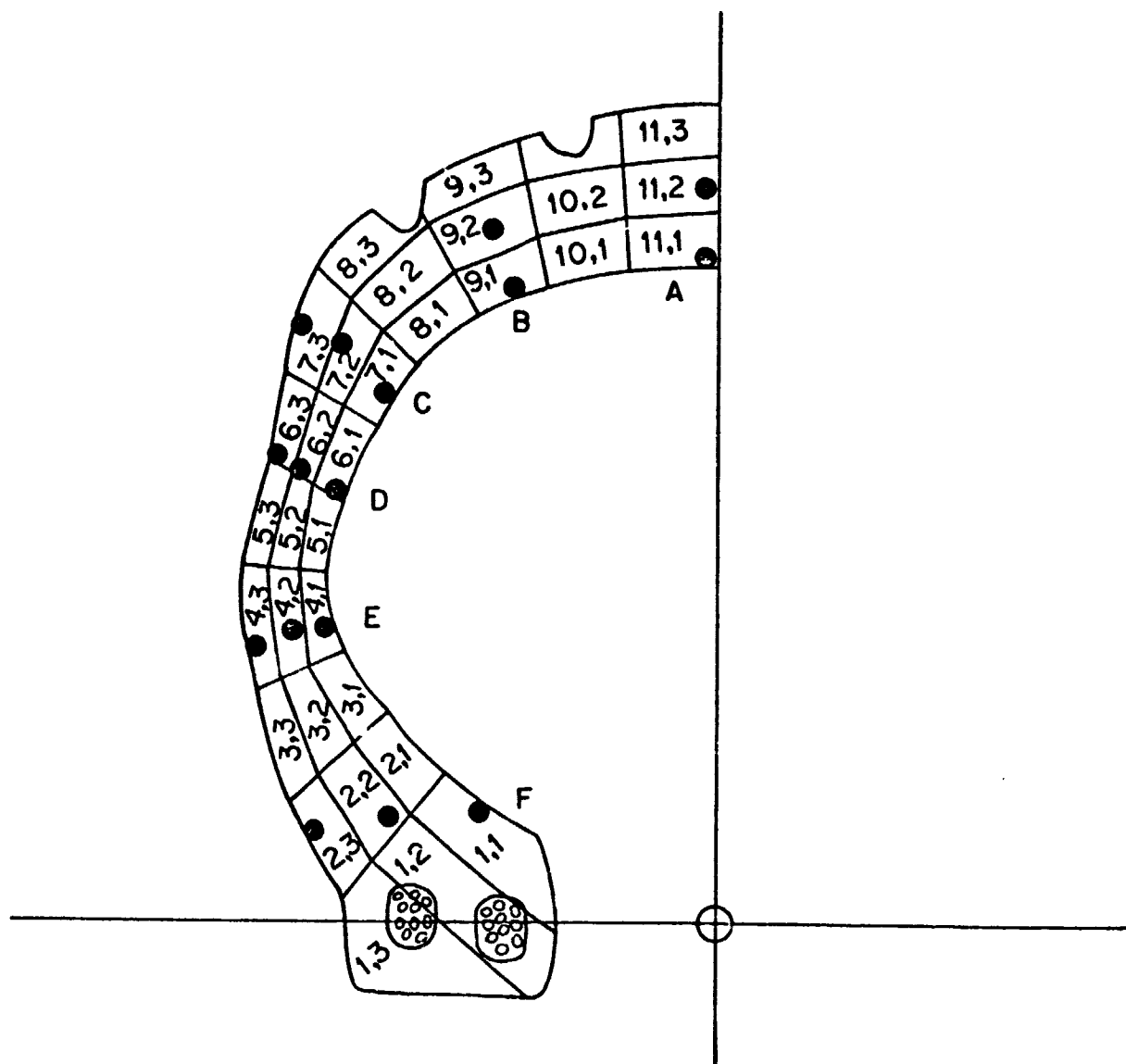


Figure H2 - Element Sectioning for Thermal Analysis
 Solid Dots Represent Approximate Location
 of Thermocouples. 22 x 5.5 12PR

Table H1 - Geometric Properties of 22x5.5 8PR

Element	LH cm ²	LV cm ²	DH cm	DV cm	Y in	YS in	AA cm ²	DA cm	AC cm ²	DC cm	R in	H1 in	H2 in
1,1	2.5	.70	.70	2.05	.10	5.74							
1,2	1.8	.70	.70	1.5	.37	5.90	-	-	2.7	.30	6.55	.80	.25
1,3	2.2	.55	-	1.2	.66	-							
2,1	1.1	.55	.65	1.2	.12	5.14							
2,2	1.05	.60	.60	1.1	.37	5.35	-	-	1.1	.30	7.12	.60	.25
2,3	1.1	.55	-	1.1	.60	-							
3,1	1.3	.35	.50	1.3	.08	4.70							
3,2	1.3	.50	.55	1.3	.29	4.95	1.3	.30	1.3	.20	7.48	.40	.11
3,3	1.4	.45	-	1.3	.49	-							
4,1	1.2	.35	.35	1.2	.05	4.20							
4,2	1.25	.35	.40	1.35	.19	4.45	1.3	.20	1.2	.15	7.90	.20	.14
4,3	1.3	.30	-	1.40	.34	-							
5,1	1.4	.25	.30	1.40	.05	3.70							
5,2	1.55	.30	.30	1.50	.16	3.95	1.7	.15	1.4	.10	8.35	.20	.15
5,3	1.70	.25	-	1.70	.28	-							
6,1	1.55	.30	.25	1.45	.04	3.18							
6,2	1.70	.35	.35	1.60	.14	3.35	2.0	.20	1.5	.10	8.90	.20	.10
6,3	1.90	.30	-	1.70	.27	-							
7,1	1.40	.30	.35	1.40	.05	2.64							
7,2	1.50	.55	.40	1.40	.18	2.75	1.8	.20	1.9	.15	9.38	.20	.28
7,3	1.70	.50	-	1.60	.33	-							
8,1	1.50	.60	.50	1.35	.07	2.00							
8,2	1.70	.60	.50	1.55	.28	2.20	1.9	.30	1.5	.20	9.78	.20	.44
8,3	1.80	.60	-	1.80	.47	-							
9,1	1.55	.55	.55	1.60	.12	1.50							
9,2	1.70	.65	.60	1.80	.34	1.59	1.9	.40	1.4	.30	10.08	.20	.50
9,3	1.90	.65	-	1.80	.54	-							
10,1	1.80	.60	.60	1.50	.10	.88							
10,2	1.80	.70	.75	1.60	.33	.91	2.0	.40	1.6	.30	10.2	.20	.55
10,3	1.20	.80	-	1.70	.62	-							
11,1	1.50	.75	.60	-	.12	.30							
11,2	1.60	.75	.70	-	.36	.33	1.7	.40	1.5	.30	10.3	.20	.60
11,3	1.70	.65	-	-	.63	-							

Table H2 - Geometric Properties of 22x5.5 12PR

Element	LH cm ²	LV cm ²	DH cm	DV cm	Y in	YS in	AA cm ²	DA cm	AC cm ²	DC cm	R in	H1 in	H2 in
1,1	2.8	.80	.80	1.9	.16	5.74	-	-	3.1	.40	6.55	.65	.55
1,2	3.2	.85	1.2	2.2	.45	5.90							
1,3	4.1	.80	.90	1.9	.90	0							
2,1	1.35	.70	.70	1.3	.15	5.14	.5	.35	1.3	.35	7.10	.70	.10
2,2	1.5	.65	.85	1.5	.43	5.35							
2,3	1.6	.65	.35	1.6	.70	0							
3,1	1.35	.55	.50	1.3	.12	4.70	1.7	.25	1.2	.25	7.56	.45	.15
3,2	1.5	.50	.60	1.5	.34	4.95							
3,3	1.65	.45	.25	1.6	.55	0							
4,1	1.4	.45	.45	1.2	.08	4.20	1.8	.20	1.3	.15	8.09	.30	.18
4,2	1.6	.45	.45	1.4	.26	4.45							
4,3	1.8	.40	.20	1.6	.44	0							
5,1	1.3	.40	.40	1.2	.08	3.70	1.6	.15	1.2	.20	8.65	.28	.20
5,2	1.4	.40	.35	1.3	.25	3.95							
5,3	1.6	.35	.15	1.4	.38	0							
6,1	1.1	.55	.45	1.1	.10	3.18	1.4	.20	1.0	.20	9.12	.28	.30
6,2	1.2	.50	.50	1.2	.27	3.35							
6,3	1.3	.55	.20	1.4	.47	0							
7,1	1.2	.65	.60	1.2	.12	2.64	1.6	.25	1.1	.30	9.58	.32	.40
7,2	1.4	.75	.60	1.3	.36	2.75							
7,3	1.6	.70	.25	1.5	.60	0							
8,1	1.4	.65	.75	1.2	.12	2.06	2.0	.35	1.2	.35	9.99	.34	.50
8,2	1.6	.80	.80	1.5	.40	2.20							
8,3	1.9	.65	.40	1.8	.70	0							
9,1	1.4	.80	.70	1.4	.14	1.50	2.0	.35	1.2	.35	10.3	.33	.48
9,2	1.6	.70	.70	1.5	.40	1.59							
9,3	1.8	.70	.30	1.5	.68	0							
10,1	1.3	.80	.75	1.3	.15	.88	2.0	.35	1.2	.40	10.5	.35	.55
10,2	1.4	.75	.75	1.4	.42	.91							
10,3	1.5	.75	.35	1.5	.70	0							
11,1	1.4	.80	.80	.70	.15	.30	1.7	.40	1.4	.40	10.6	.35	.56
11,2	1.5	.80	.75	.70	.46	.33							
11,3	1.5	.80	.40	.70	.75	0							

Section Height = 4.1 in.

APPENDIX I

Thermal Analysis

In the thermal analysis discussed below account is taken of conduction to neighboring elements, conduction to the road surface, convection to the outside air and to the inside air, and heat generation within each element. In writing the heat balance equation for each element it is necessary to provide effective heat transfer and heat generation coefficients for each element. The necessary coefficients are:

$$AV, AH = \frac{K_R \cdot a \cdot \Delta t}{C_R \cdot \rho_R \cdot v \cdot d}$$

$$QB = \frac{\dot{q} \cdot v \cdot \Delta t}{C_R \cdot \rho_R \cdot v}$$

$$HR = \frac{1}{\frac{\frac{1}{K_R \cdot a}}{C_R \cdot \rho_R \cdot v \cdot d} + \frac{\frac{1}{h_R \cdot a}}{C_R \cdot \rho_R \cdot v}}$$

$$HA = \frac{1}{\frac{\frac{1}{K_R \cdot a}}{C_R \cdot \rho_R \cdot v \cdot d} + \frac{\frac{1}{h_A \cdot R_i \cdot a}}{\frac{R_1}{C_R \cdot \rho_R \cdot v}}}$$

$$HC = \frac{1}{\frac{\frac{1}{K_R \cdot a}}{C_R \cdot \rho_R \cdot v \cdot d} + \frac{\frac{1}{h_c \cdot a}}{C_R \cdot \rho_R \cdot v}}$$

$$HF = \frac{1}{\frac{1}{\frac{K_R \cdot a}{C_R \rho_R \cdot v \cdot d}} + \frac{1}{\frac{K_A \cdot a}{C_A \rho_A \cdot v d}} + \frac{1}{\frac{h_f \cdot a}{C_R \rho_R \cdot v}}}$$

where:

- AV, AH - effective heat conduction coefficeints, neighboring elements
- QB - effective heat generation coefficient, each element
- HF - effective heat transfer coefficient, tire-rim interface
- HR - effective heat transfer coefficient, tire-road interface
- HA - effective heat transfer coefficient, tire-outside air interface
- HC - effective heat transfer coefficient, tire-contained air interface

- v = volume of each element - see Table A
- a = area across which heat is transferred - see Table A
- d = distance between nodes - see Table A
- Δt = time increment - selected
- q = rate of heat generation each element - see earlier sections
- K_R = thermal conductivity of rubber = 5×10^{-4} cal·cm/°C·cm²·sec
- K_A = thermal conductivity of rim = .48 cal·cm/°C·cm²·sec
- C_R = specific heat of rubber = 0.5 cal/gm °C
- C_A = specific heat of rim = .23 cal/gm °C
- ρ_R = density of rubber = 1 gm/cm³
- ρ_A = density of rim = 2.7 gm/cm³
- h_R = film heat transfer coefficient, tire-road interface
= .25 cal/°C·cm²·sec
- h_A = film heat transfer coefficient, tire-outside air inter-
face = $(1.3 \times 10^{-4} + 4 \times 10^{-7} V(\text{cm/sec}))$ cal/°C·cm²·sec
- h_C = film heat transfer coefficient, tire-contained air
interface = 1×10^{-4} cal/°C·cm²·sec
- h_f = film heat transfer coefficient, tire-rim interface
= .5 cal/°C cm²·sec

Typical heat balance equations for the individual elements of the 22x5.5 8PR tire are listed below where each equation has been solved for the change in temperature which takes place during a given increment of time.

The inside elements all have an equation of the form:

$$\begin{aligned}\Delta T_{I,1} = & QB(I,1) + AH(I,1)(T_{I,2} - T_{I,1}) + AV(I,1)(T_{I+1,1} - T_{I,1}) \\ & + AV(I-1,1)(T_{I-1,1} - T_{I,1}) + HC(I)(TC - T_{I,1})\end{aligned}$$

The middle elements all have an equation of the form:

$$\begin{aligned}\Delta T_{I,2} = & QB(I,2) + AH(I,2)(T_{I,3} - T_{I,2}) + AH(I,1)(T_{I,1} - T_{I,2}) \\ & + AV(I,2)(T_{I+1,2} - T_{I,2}) + AV(I-1,2)(T_{I-1,2} - T_{I,2})\end{aligned}$$

The outside elements not in contact with the road surface or rim have an equation of the form:

$$\begin{aligned}\Delta T_{I,3} = & QB(I,3) + AH(I,2)(T_{I,2} - T_{I,3}) + AV(I,3)(T_{I+1,3} - T_{I,3}) \\ & + AV(I-1,3)(T_{I-1,3} - T_{I,3}) + HA(I)(TA - T_{I,3})\end{aligned}$$

The outside elements in contact with the rim have the same form except HA is replaced by HF and TA by TF.

The outside elements in the tread region are assumed to be in contact with the air 90% of the time and in contact with the road surface 10% of the time. The heat balance equation for these elements is of the form:

$$\begin{aligned}\Delta T_{I,3} = & QB(I,3) + AH(I,2)(T_{I,2} - T_{I,3}) + AV(I,3)(T_{I+1,3} - T_{I,3}) \\ & + AV(I-1,3)(T_{I-1,3} - T_{I,3}) + 0.9 HA(I)(TA - T_{I,3}) \\ & + 0.1 HR(I)(TR - T_{I,3})\end{aligned}$$

In this analysis the outside air temperature T_A , the rim temperature T_F , and the road surface temperature T_R are assumed to remain constant. However, the change in the contained air temperature T_C is approximated as follows:

$$\Delta T_C = \frac{h_c \cdot A \cdot \Delta t \cdot (\bar{T}_i - T_C)}{C_c \rho_c \cdot V}$$

where:

$$C_c = .24 \text{ cal/gm}^\circ \text{C}$$

$$\rho_c = .0013 \text{ gm/cm}^3$$

$$\bar{T}_i = \text{weighted average of inside surface temperatures}$$

For the 22x5.5 8PR tire analyzed, the approximate values of A and V are 30.4 cm^2 and 90.35 cm^3 , respectively. Thus, for this tire:

$$\Delta T_C = .1078(\bar{T}_i - T_C) \cdot \Delta t$$